Banner appropriate to article type will appear here in typeset article

Effect of subgrid-scale anisotropy on wall-modeled large-eddy simulation of separated flow

Di Zhou 1,2† and H. Jane Bae 1

¹Graduate Aerospace Laboratories, California Institute of Technology, Pasadena, CA 91125, USA
²Department of Mechanical and Aerospace Engineering, University of Tennessee, Knoxville, TN 37996, USA

(Received xx; revised xx; accepted xx)

We examine the role of anisotropic subgrid-scale (SGS) stress in wall-modeled largeeddy simulation (WMLES) of flow over a spanwise-uniform Gaussian-shaped bump, with particular emphasis on predicting flow separation. The simulations show that eddy-viscositybased SGS models often yield non-monotonic predictions of the mean separation bubble size on the leeward side under grid refinement, whereas models incorporating anisotropic SGS stress produce more consistent results across mesh resolutions. To identify where SGS anisotropy is most critical, we selectively introduce anisotropic SGS terms in different regions of the computational domain. The results reveal that the windward side near the bump peak, where a strong favorable pressure gradient (FPG) occurs, plays a crucial role in determining downstream flow separation. Analysis of the Reynolds stress transport equation shows that fluctuations of anisotropic SGS stress directly modify SGS dissipation and diffusion in this region, thereby altering the Reynolds stress distributions and the onset of downstream separation. Examination of the mean streamwise momentum equation indicates that at coarse resolutions, the mean SGS shear stress dominates, and the differences between the eddy-viscosity-based and anisotropic models remain minor. As the grid is refined, however, resolved Reynolds stresses increasingly govern the near-wall momentum transport, and the influence of SGS stress fluctuations becomes more pronounced, as they determine the SGS dissipation and diffusion of Reynolds stresses. Component-wise analysis of the SGS stress tensor further shows that the improvement arises mainly from including significant normal stress contributions. Finally, an a priori study using filtered direct numerical simulation (DNS) of turbulent Couette-Poiseuille flow confirms that wall-bounded turbulence under FPG is highly anisotropic and that anisotropic SGS models provide a more realistic representation of SGS stress anisotropy than eddy-viscosity-based models.

MSC Codes 76F65, 76F40

1. Introduction

Complex turbulent flows with separation are commonplace in various aerodynamic and hydrodynamic vehicles, significantly influencing their performance and stall characteristics. The ability to accurately predict such flows is therefore crucial for the design and assessment

† Email address for correspondence: dzhou6@utk.edu

of these systems. A potentially suitable and feasible tool for this purpose is wall-modeled large-eddy simulation (WMLES) (Larsson et al. 2016; Park 2017; Bose & Park 2018), as it resolves the energy-containing and dynamically important scales of turbulence away from the wall while employing a reduced-order model to account for the effects of energetic near-wall eddies. Compared with classical wall-resolved large-eddy simulation (WRLES), WMLES not only significantly reduces the grid resolution requirement but also allows for a larger time-step sizes; therefore, it is computationally more efficient. Recent studies (Choi & Moin 2012; Yang & Griffin 2021) have shown that the computational cost of WMLES is one to two orders of magnitude smaller than that for the WRLES in attached flow over a finite aspect-ratio wing at varying Reynolds numbers. Because of these advantages, WMLES has been anticipated as the next step toward the broader use of high-fidelity simulation in realistic engineering applications. In recent years, WMLES has been applied to complex flow configurations in practical engineering contexts (Lehmkuhl et al. 2018; Goc et al. 2021, 2024). These simulations have highlighted the capability of WMLES in predicting critical flow-performance quantities, particularly in comparison with approaches based on Reynoldsaveraged Navier-Stokes (RANS) closures. Moreover, by leveraging modern, massively parallel computer architectures, these simulations achieve turnaround times of less than a few days with modest computational resources.

Currently, the primary challenge in applying WMLES to realistic applications lies in achieving both robustness and accuracy across a range of flow regimes and configurations. However, many existing wall models are built upon the assumption of statistically equilibrium wall-bounded turbulence, which applies to only a limited class of turbulent flows. To go beyond the equilibrium assumption, developing more capable techniques that can address a wider range of non-equilibrium flows has become a key focus within the wall-modeling community. A widely used approach has been to develop wall models based on the thin boundarylayer equations while incorporating some or all of the effects of unsteadiness, convection, and pressure gradients (Wang & Moin 2002; Kawai & Larsson 2013; Park & Moin 2014). An alternative approach is dynamic slip wall modeling (Bose & Moin 2014; Bae et al. 2019), which is derived directly from the filtered Navier-Stokes equations instead of relying on thin boundary-layer approximations. Despite these advancements in wall modeling techniques, accurate numerical prediction of complex separated flows remains a significant challenge for WMLES. Recent studies (Lozano-Durán & Bae 2019; Rezaeiravesh et al. 2019; Zhou & Bae 2024a) have demonstrated that this challenge arises not only from the less-than-ideal performance of wall-modeling approaches but also, and perhaps more importantly, from the insufficient capability of existing subgrid-scale (SGS) models in WMLES, a topic that has received relatively little attention. Specifically, Zhou et al. (2023) and Zhou & Bae (2024a) have shown that the influence of SGS models on WMLES of turbulent flow with separation is profound, significantly limiting the robustness and applicability of WMLES.

In large-eddy simulations (LES), the large scales of turbulent flow are explicitly resolved, while the effects of small-scale motions are modeled using SGS models. It is often assumed that turbulence at the small, unresolved scales is largely isotropic. Based on this assumption, the original development of SGS models focused on WRLES using fine-resolution computational meshes, and the effects of SGS were modeled using simple isotropic models such as eddy-viscosity models. However, computational meshes with much coarser resolution employed in WMLES were not fully considered in the development of SGS models. To date, eddy-viscosity models still represent the most commonly used class of SGS models in LES (Moser *et al.* 2021; Duraisamy 2021; Choi *et al.* 2025). While they can provide a statistically accurate energy transfer rate from resolved scales to SGS (*i.e.*, dissipation of kinetic energy), several studies (Clark *et al.* 1979; Kerr *et al.* 1996; Domaradzki & Saiki 1997) have highlighted that the output of these models is poorly

correlated with the exact SGS stress computed from direct numerical simulation (DNS). Beyond dissipation, there are statistical characteristics that the SGS model must satisfy to enable reliable simulations (Moser *et al.* 2021), for example, accurately predicting the mean SGS stress. Unfortunately, investigations (Meneveau 1994; Jimenez & Moser 2000; Li & Meneveau 2004) have shown that eddy-viscosity models may not sufficiently capture both the energy transfer and SGS stress behavior in turbulent flows. It has also been observed that eddy-viscosity models produce a non-monotonic convergence behavior for separation bubble prediction at coarser mesh resolutions (Whitmore *et al.* 2021; Agrawal *et al.* 2022; Zhou & Bae 2024*a*). Consequently, they often require the LES resolution to be fine enough for the mean SGS stress to become negligible. This reliance on finer resolution limits their practical applicability, underscoring the need for SGS models compatible with WMLES that can still yield accurate predictions of complex turbulent flows.

The central challenge in advancing SGS models is overcoming the so-called well-resolved barrier, where the majority of turbulence is adequately captured. For coarser resolutions, SGS models must fulfill roles beyond simple energy dissipation, as subgrid motions contribute increasingly to mean momentum and energy transport. Moreover, the effects of SGS anisotropy, both in dissipation and stress, cannot be ignored, especially at the smallest resolved scales that are dynamically active and energy-containing. The primary limitation of traditional eddy-viscosity models arises from their single degree of freedom, which restricts their ability to represent both stress and dissipation simultaneously. Reliable WMLES at coarse resolutions therefore requires enhanced formulations beyond the isotropic models to represent both stress and dissipation simultaneously. To achieve these goals, a variety of anisotropic SGS models have been proposed over the past decades, including mixed similarity models (Zang et al. 1993; Liu et al. 1994; Vreman et al. 1994, 1997; Horiuti 1997; Meneveau & Katz 2000; Kobayashi & Shimomura 2001; Inagaki & Kobayashi 2020; Iyer & Malik 2024), algebraic models (Gatski & Jongen 2000; Marstorp et al. 2009; Rasam et al. 2017; Montecchia et al. 2017; Silvis & Verstappen 2019), and other nonlinear SGS models (Wang & Bergstrom 2005; Abe 2013, 2014; Vollant et al. 2016; Kobayashi 2018; Agrawal et al. 2022; Uzun & Malik 2025). These models have been shown to outperform traditional eddy-viscosity models in canonical turbulent flows such as channel flows and turbulent boundary layers (TBLs). However, their performance in more complex and realistic configurations remains insufficiently explored. Furthermore, despite the wide range of proposed models, detailed analyses of their underlying mechanisms and the effects of SGS anisotropy are still limited. It is therefore necessary to investigate the effects of anisotropic SGS stress in complex turbulent flows, particularly as model development in this area has progressed relatively slowly.

Investigations into the effect of anisotropic SGS stress have recently gained momentum. Several studies have focused on *a priori* analyses (Horiuti 2003; Abe 2019; Cimarelli *et al.* 2019; Inagaki & Kobayashi 2023) based on filtered DNS data, showing that SGS anisotropy significantly influences the evolution of Reynolds stress, vorticity, and enstrophy, particularly in wall-bounded turbulence. However, previous studies (Vreman *et al.* 1997; Park *et al.* 2005; Duraisamy 2021; Choi *et al.* 2025) on both traditional and data-driven SGS models have revealed inconsistencies between the results of *a priori* and *a posteriori* evaluations. Specifically, models that perform poorly in *a priori* tests may yield excellent *a posteriori* results, and vice versa, highlighting a fundamental limitation of the *a priori* analysis. Given this gap, and to fully evaluate the effects of anisotropic SGS stress on WMLES of separated turbulent flows, we conduct a comprehensive *a posteriori* study.

In particular, this *a posteriori* investigation focuses on the flow over a Gaussian-shaped bump at a relatively high Reynolds number (see figure 1), as proposed by Boeing Research & Technology (Slotnick 2019). This configuration is closely related to realistic applications,

mimicking the smooth junctions between an aircraft wing and fuselage, where smoothbody separation of a TBL occurs under the combined influence of pressure gradients and surface curvature. As a canonical flow configuration, it has been extensively studied, and a wealth of experimental data is available (Williams et al. 2020; Gray et al. 2021, 2022a,b; Gluzman et al. 2022), establishing it as a benchmark for validating computational fluid dynamics techniques (Balin & Jansen 2021; Whitmore et al. 2021; Iyer & Malik 2022; Agrawal et al. 2022; Uzun & Malik 2022; Arranz et al. 2023; Zhou et al. 2023; Zhou & Bae 2024b; Agrawal et al. 2024; Iyer & Malik 2025). Computational studies have consistently emphasized the challenge of accurately predicting the extent and location of separation on the leeward side of the bump. Recent WMLES studies have shown that mean separation prediction is highly sensitive to the SGS model employed, affecting both accuracy and robustness (Iyer & Malik 2022; Agrawal et al. 2022; Zhou & Bae 2024a). Furthermore, anisotropic SGS models have been found to markedly improve the predictions of mean velocity field in WMLES (Agrawal et al. 2022; Zhou & Bae 2024a; Iyer & Malik 2024; Uzun & Malik 2025). Given the complex physics of smooth-body separation and the sensitivity of its separation prediction to the SGS model, the flow over a Gaussian-shaped bump is an ideal test case for the present a posteriori analysis. To avoid the complexities due to spanwise variations, this study focuses on a spanwise-uniform Gaussian bump with periodic boundary conditions in the spanwise direction. The flow configuration and simulation setup follow the hybrid DNS-WRLES study by Uzun & Malik (2022), which also provides high-fidelity reference data. Through this study, we aim to improve understanding of how anisotropic SGS models influence the statistics and dynamics of separated flow in WMLES, particularly the mean velocity field and the onset of smooth-body separation. We also seek to characterize the properties of anisotropic SGS stress and identify key features required of SGS models for accurate and robust WMLES in complex separated flows. Building on these insights, our ultimate goal is to provide guidance for future SGS model development and enhance the overall predictive performance of WMLES.

The remainder of the paper is organized as follows. §2 describes the numerical approach, flow configuration, and simulation setup, including computational meshes and boundary conditions. In §3, the sensitivity of mean flow separation to the SGS models and grid resolution is examined through a series of WMLES, and a numerical experiment that introduces anisotropic SGS stress in different regions of the computational domain is conducted to identify where SGS anisotropy is most critical. §4 presents detailed analyses based on the simulation data to explain the mechanisms underlying the sensitivities of the flow separation prediction, as well as the role of the anisotropic SGS stress in the flow over the Gaussian bump. Specifically, the budgets of the mean streamwise momentum and Reynolds stress transport equations are examined. In §5, the properties of the SGS stress in these simulations are then investigated and compared with corresponding results from an *a priori* study based on filtered DNS data of a turbulent Couette–Poiseuille flow. Finally, §6 summarizes the key findings and provides insights for further improvement of the WMLES technique.

2. Computational methodology

2.1. Numerical approach

Flow simulations are conducted employing a finite-volume, unstructured-mesh LES code (You *et al.* 2008). The reliability of this LES code in accurately simulating turbulent flows has been demonstrated in various configurations, such as rough-wall TBLs (Yang & Wang 2013), flow over an axisymmetric body of revolution (Zhou *et al.* 2020), and rotor interactions with

thick axisymmetric TBL (Zhou *et al.* 2024). In this LES code, the spatially-filtered incompressible Navier-Stokes equations are solved with second-order accuracy using cell-based, low-dissipative, and energy-conservative spatial discretization and a fully implicit, fractional-step time-advancement method with the Crank–Nicolson scheme. The Poisson equation for pressure is solved using the bi-conjugate gradient stabilized method (Van der Vorst 1992). The governing equations for LES of incompressible turbulent flows are given by

$$\frac{\partial \tilde{u}_i}{\partial x_i} = 0, (2.1)$$

and

$$\frac{\partial \tilde{u}_i}{\partial t} + \tilde{u}_j \frac{\partial \tilde{u}_i}{\partial x_j} = -\frac{1}{\rho} \frac{\partial \tilde{p}}{\partial x_i} + \nu \frac{\partial^2 \tilde{u}_i}{\partial x_j \partial x_j} - \frac{\partial}{\partial x_i} \tau_{ij}^{\text{sgs}}, \tag{2.2}$$

where u_i is the instantaneous flow velocity, p is the instantaneous static pressure, ρ is fluid density, ν is fluid kinematic viscosity and $\widetilde{(\cdot)}$ denotes grid-filtering operation. SGS stress is given by the tensor $\tau_{ij}^{\rm sgs} = \widetilde{u_i u_j} - \widetilde{u_i} \widetilde{u_j}$. The deviatoric part of the SGS stress tensor is modeled using an SGS model for closure of the equations, and the isotropic component of the SGS stress is absorbed into pressure. Without specific description, the SGS stress term in the following discussion denotes the deviatoric part of the corresponding SGS stress tensor. Additionally, in the following discussions, the tilde symbol, which denotes the grid filtering operation, will be omitted for the sake of simplicity. Hence, u_i and p will directly represent the instantaneous physical quantity of resolved flow field.

In the current study, two SGS models are investigated. The first model is the classical Smagorinsky model (SM) (Smagorinsky 1963), a widely used isotropic SGS model based on the eddy-viscosity closure assumption. The corresponding SGS stress is given by

$$\tau_{ij}^{\text{sgs}} = \tau_{ij}^{\text{SM}} = -2(C_s \Delta)^2 |S| S_{ij} , \qquad (2.3)$$

where S_{ij} represents the strain-rate tensor, and $|S| = (2S_{ij}S_{ij})^{1/2}$. Furthermore, in the Smagorinsky model, the eddy viscosity is represented by $v_t = (C_s \Delta)^2 |S|$, where Δ denotes the grid filter width, typically assumed to be the geometric mean of the local grid size. The Smagorinsky coefficient, C_s , is typically between 0.1 and 0.2. In the present study, we use $C_s = 0.16$, which was originally calibrated for homogeneous isotropic turbulence. The second SGS model is an anisotropic SGS model that consist of the isotropic term τ_{ij}^{iso} given by the SM (Smagorinsky 1963) and an additional anisotropic SGS stress term τ_{ij}^{ani} , such that

$$\tau_{ij}^{\text{sgs}} = \tau_{ij}^{\text{iso}} + \tau_{ij}^{\text{ani}} = \tau_{ij}^{\text{SM}} + \tau_{ij}^{\text{ani}}$$
 (2.4)

Specifically, we consider a modified SM (MSM), where the anisotropic SGS stress term is defined as $\tau_{ij}^{\rm ani} = C_a \Delta^2(S_{ik}R_{kj} - R_{ik}S_{kj})$, and R_{ij} denotes the rotation-rate tensor. This anisotropic term is one of the six independent terms that arise when expanding the SGS stress in terms of the strain-rate and rotation-rate tensors (Lund & Novikov 1992; Gatski & Jongen 2000). It is explicitly incorporated in several recently developed anisotropic SGS models (Agrawal *et al.* 2022; Uzun & Malik 2025), which have shown promising predictions for flow over a Gaussian bump. Furthermore, this anisotropic term does not directly contribute to energy transfer between resolved scale and SGS (Lund & Novikov 1992; Silvis & Verstappen 2019; Inagaki & Kobayashi 2023), thus the corresponding SGS dissipation of kinetic energy is $\tau_{ij}^{\rm ani}S_{ij}=0$. This anisotropic term allows us to study the physical properties of the anisotropic SGS stress in addition to the energy transfer. To reduce the influence of different kinetic energy dissipation from these SGS models, we set $C_s=0.16$ for the MSM as well. Tests with different C_a values ranging from -1/30 to -1/6 showed no significant difference

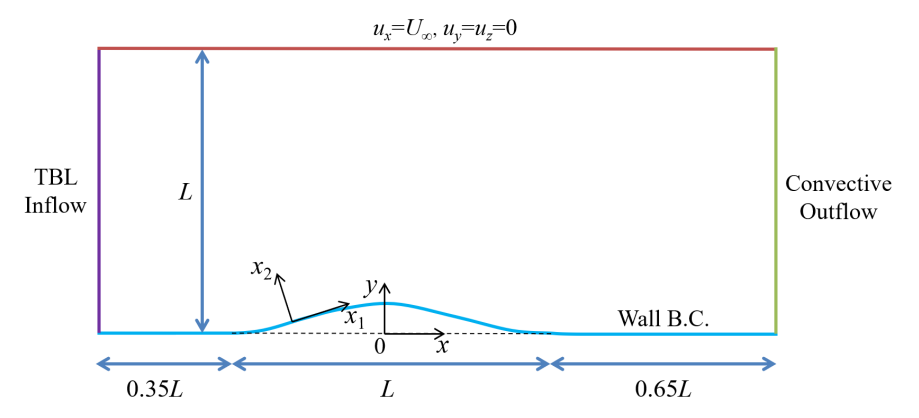


Figure 1: Simulation set-up for flow over a Guassian-shaped bump.

in the predicted separation bubble on the leeward side of the bump. Therefore, C_a in the MSM is chosen arbitrarily as -1/30, which yields the smallest modification to the SM and avoids any optimization for the flow simulations. Moreover, it should be noted that since the current study focuses on WMLES with relatively coarse meshes, damping function for eddy viscosity is not employed in the near-wall region for neither the SM or the MSM model.

2.2. Flow configuration and simulation set-up

The physical conditions for the present simulations are consistent with those in the hybrid DNS-WRLES of Uzun & Malik (2022). The flow configuration and boundary conditions are shown schematically in figure 1. The geometry of the bump is given by the analytic function $y = f_b(x) = h \exp\left[-(x/x_0)^2\right]$, where f_b is the surface representing the geometry of the wall-mounted bump, the maximum height of the bump is h = 0.085L, $x_0 = 0.195L$, and L is the width of the bump. The Reynolds number is $Re_L = U_\infty L/v = 2 \times 10^6$ based on the free-stream velocity U_∞ and the width of the bump, which is identical to that in the referenced DNS (Uzun & Malik 2022).

Simulations are conducted in a rectangular domain of length 2L, height L and spanwise depth 0.08L. The dimensions in the vertical and spanwise directions are chosen to be the same values as those in the DNS of Uzun & Malik (2022). For convenience, both a Cartesian coordinate system (x-y-z) with velocity components (u, v, w) and a localized coordinate system $(x_1-x_2-x_3)$ with velocities (u_1, u_2, u_3) are used simultaneously in this paper, and both coordinates obey the right-hand rule. Specifically, the x-y-z system is defined as a global coordinate system. The origin is placed at the base of the bump peak, which is located 0.85L downstream from the inlet, as shown in figure 1. In the localized system, x_1 is tangential to the bump surface in the flow direction, x_2 is normal to the surface and points toward the flow field, and x_3 is identical to the spanwise direction z. Correspondingly, u_1 is the local streamwise velocity, u_2 is the local wall-normal velocity, u_3 is identical to the spanwise velocity u_z .

The boundary conditions consist of a TBL inflow at the inlet, free-stream condition on the top boundary, convective outflow condition at the exit, and periodic conditions on the spanwise boundaries. The TBL inflow data for the simulations of flow over Gaussian bump are provided by a separate LES of flat-plate TBL using the rescale-and-recycle method of Lund *et al.* (1998). The friction Reynolds number Re_{τ} of the TBL inflow is approximately equal to 620 and the TBL thickness is $\delta_{\rm in}/L=0.0061$, which is approximately 10% larger than that in the DNS of Uzun & Malik (2022). The momentum thickness Reynolds number of the inflow is $Re_{\theta} \approx 1074$, compared to their slightly smaller value of approximately 1035.

Mesh label	$\Delta_{ m c}/L$	Cell number
Coarsest mesh	1.90×10^{-3}	$1050 \times 44 \times 42 \approx 1.94$ million
Coarse mesh	9.52×10^{-4}	$2100 \times 88 \times 84 \approx 15.5$ million
Medium mesh	4.76×10^{-4}	$4200 \times 176 \times 168 \approx 124$ million
Fine mesh	2.38×10^{-4}	$8400 \times 352 \times 336 \approx 993$ million

Table 1: Parameters of the computational meshes utilizing isotropic cells.

More details of the TBL inflow and the corresponding simulation are refereed to our previous publication (Zhou & Bae 2024a). Additionally, it should be noted that the inflow-generation method used in the study of Uzun & Malik (2022) is different from the current method. The current study focuses on investigating the SGS model effect on WMLES, thus in order to sidestep the complexity associated with the modeling of wall-shear stress and its interaction with the SGS model, the physical no-slip condition at the solid surface is replaced by an ideal boundary condition based on the mean wall-shear stress from DNS. Specifically, it adopts a time-independent Neumann boundary condition given by the form

$$\left. \left(\frac{\partial u_1}{\partial x_2} \right) \right|_{w} = \frac{\tau_{w,1}^{\text{DNS}}}{\rho \nu} , \qquad (2.5)$$

where $\tau_{w,1}^{\text{DNS}}$ is the mean wall-shear stress known *a priori* from the DNS (Uzun & Malik 2022), μ is the fluid dynamic viscosity, and the subscript w denotes the quantities evaluated at the solid wall. This boundary condition can be treated as an idealized wall model supplying the exact mean wall-shear stress. The distribution of the mean skin-friction coefficient on the bottom solid surface can be referred to the paper of Uzun & Malik (2022). Meanwhile, a no-penetration condition is enforced at the solid surface for the wall-normal velocity u_2 .

The computational mesh consists of structured-mesh blocks around the bottom surface and unstructured-mesh blocks in the outer region. To avoid resolution-induced anisotropy (Haering et al. 2019) and to more clearly analyze the effect of mesh resolution, we used isotropic computational meshes with increasing resolutions within the structured-mesh block. The parameters of these computational meshes are detailed in Table 1, which are identical to those computational meshes employed in our previous investigation (Zhou & Bae 2024a). Based on the TBL thickness at x/L = -0.65 from the DNS of Uzun & Malik (2022), the TBL is resolved by approximately 5 cells in the coarsest mesh, 9 cells in the coarse mesh, 18 cells in the medium mesh, and 36 cells in the fine mesh. In particular, the resolution of the fine mesh, determined based on the mesh-cell size and the mean skin friction from the reference DNS (Uzun & Malik 2022), ranges from 10 to 30 wall units within regions of attached flow. Although this resolution is comparable to that of the standard WRLES mesh in the streamwise and spanwise directions, it is order of magnitude coarser in the wall-normal direction within the near-wall region. For the DNS computational mesh (Uzun & Malik 2022), the characteristic cell size Δ_c , which is the geometric mean of the mesh cell dimension, is approximately equal to $1.10 \times 10^{-4} L$. This estimate is derived from the mesh resolution at the location of the thickest separation bubble. In the outer unstructured-mesh blocks of the current computational meshes, the mesh cell size is smaller than 0.1L, and the control volumes are gradually refined towards the bottom surface.

A maximum Courant–Friedrichs–Lewy number of 1.0 is used for time advancement in all simulations. The simulations are first run for two flow-through times $(4L/U_{\infty})$ to wash out

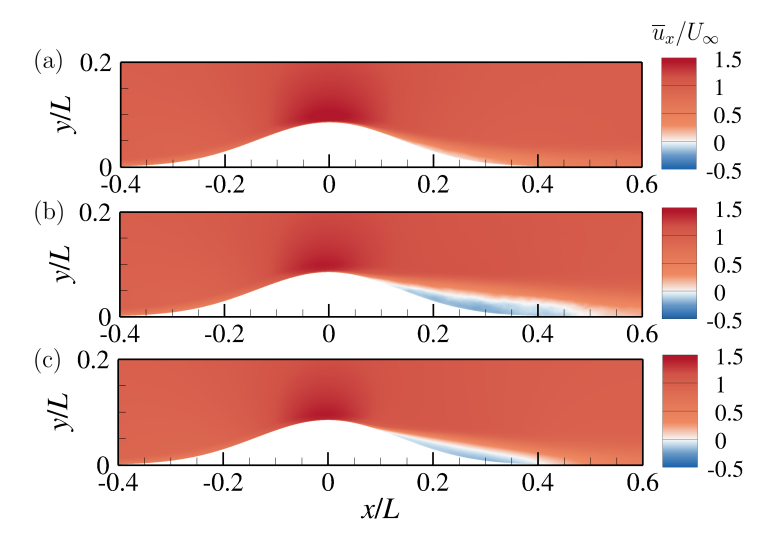


Figure 2: Isocontours of mean velocity \overline{u}_x/U_∞ from the medium-mesh simulations with the SM (a) and MSM (b) and from the reference DNS (Uzun & Malik 2022) (c).

initial transients, and then another three flow-through times $(6L/U_{\infty})$ to obtain converged statistics.

3. Sensitivity of mean flow separation prediction to SGS model

3.1. Separation prediction and grid convergence test

The flow field around the Gaussian-shaped bump, obtained using the medium mesh for the two SGS models, is shown in figure 2. Here, $\overline{(\cdot)}$ denotes both temporal averaging and spatial averaging along the homogeneous directions. With this definition, an instantaneous quantity φ can be decomposed as $\varphi = \overline{\varphi} + \varphi'$. For reference, the DNS results from Uzun & Malik (2022) are also included in the figure.

In the DNS flow field, the incoming TBL accelerates upstream of the bump peak and then decelerates downstream under the influence of an adverse pressure gradient (APG), leading to rapid thickening of the boundary layer on the leeward side. Farther downstream, a pronounced separation bubble forms. In contrast, for the present medium-mesh WMLES, the predicted separation behavior is highly sensitive to the SGS model. The simulation using the SM does not predict any flow separation, whereas the simulation using the MSM exhibits a separation bubble that is larger than the one observed in the DNS.

The contours of the mean eddy viscosity in SGS model, denoted by $\overline{\nu}_t/\nu$, from the mediummesh simulations in an x-y plane are shown in figure 3. For the MSM, the eddy viscosity arises solely through the isotropic stress term of the Smagorinsky model, as defined in Eq. 2.4. The magnitude of the eddy viscosity within the TBL is on the same order of magnitude as the fluid viscosity. Upstream of the bump peak, the eddy viscosity produced by the two SGS models are similar. However, farther downstream, noticeable differences emerge. In particular, although the MSM uses the same model coefficient C_s as the SM, the eddy viscosity distribution on the leeward side of the bump is significantly modified by the additional anisotropic stress term. The change in eddy viscosity indicates the SGS dissipation of kinetic energy introduced by the MSM differs substantially from that of the SM in this region.

In figure 4, the distribution of the mean pressure coefficient, $C_p = (\overline{p}_w - P_\infty)/(\frac{1}{2}\rho U_\infty^2)$,

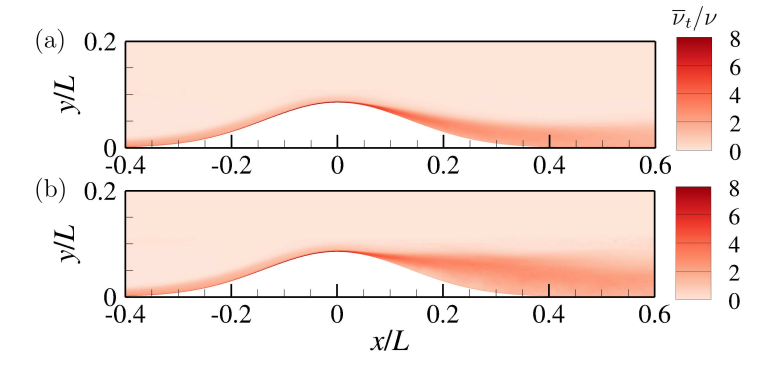


Figure 3: Isocontours of mean eddy viscosity $\overline{\nu}_t/\nu$ from the medium-mesh simulations with the SM (a) and MSM (b).

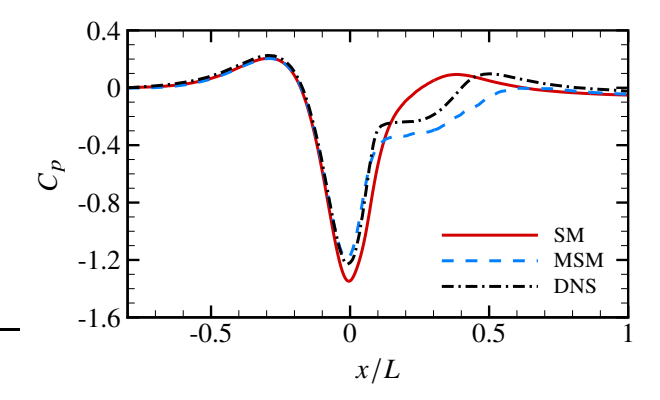


Figure 4: Mean pressure coefficient on the bottom surface from the medium-mesh simulations with the SM and MSM along with the reference DNS (Uzun & Malik 2022).

on the bottom surface is compared with the DNS data (Uzun & Malik 2022). Here, $p_{\rm w}$ denotes the instantaneous static pressure at the wall, and the reference pressure P_{∞} is taken near the top boundary at the inlet. The C_p distributions obtained from the medium-mesh simulations show a strong favorable pressure gradient (FPG) on the windward side of the bump near the bump peak. Downstream of the peak, the flow experiences a strong APG, followed by a milder APG over the majority of the leeward side. For the two medium-mesh simulations, the results agree reasonably well upstream of the bump peak and in the flat region downstream of the bump, but clear differences appear near the peak and along the leeward side. The comparison indicates that the MSM provides better agreement with the DNS data. In particular, the MSM predicts a plateau in C_p on the leeward side of the bump, corresponding to the presence of a separation bubble.

A comparison of boundary layer profiles from the medium-mesh simulations with the DNS results of Uzun & Malik (2022) is shown in figure 5, where the mean streamwise velocity \overline{u}_1 is plotted at seven streamwise stations in the computational domain. The results capture the flow acceleration on the windward side of the bump, followed by deceleration and boundary-layer thickening or separation on the leeward side. Upstream of the bump peak, the simulations employing the two SGS models agree reasonably well with each other and with the DNS data (Uzun & Malik 2022). Downstream of the peak, however, clear differences emerge. In particular, the boundary layer thickens more rapidly in the MSM simulation, leading to the



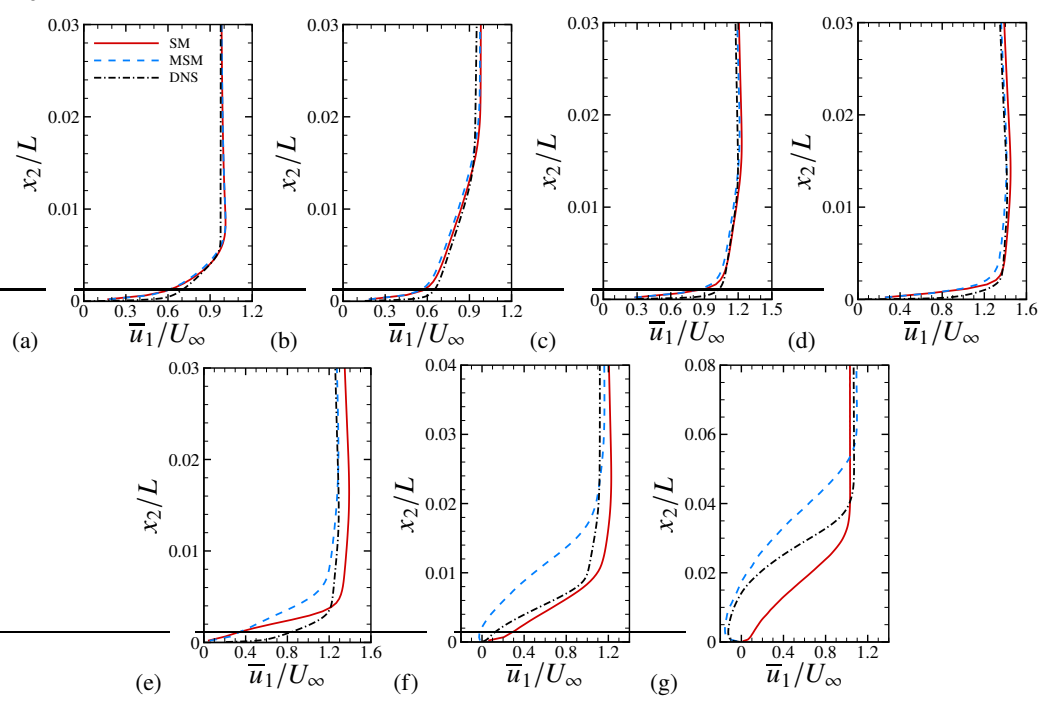


Figure 5: The profiles of mean streamwise velocity at x/L = -0.7 (a), x/L = -0.2 (b), x/L = -0.1 (c), x/L = 0 (d), x/L = 0.05 (e), x/L = 0.1 (f) and x/L = 0.2 (g) for the SM, MSM, and the reference DNS (Uzun & Malik 2022).

formation of a separation bubble, while the boundary layer in the SM simulation remains attached throughout the domain.

Since all simulations impose a wall-shear stress matched to the local mean wall-shear stress from the reference DNS (Uzun & Malik 2022), the length of the predicted separation bubble is estimated using the mean streamwise velocity at the first off-wall cell center, as shown in figure 6. A closer examination of the mean velocity distributions reveals noticeable differences between the two medium-mesh simulations. Upstream of the bump peak, the mean velocity at the first off-wall cell center agrees well across all simulations. Downstream of the peak, however, the flow in the SM simulation approaches separation but remains attached, whereas the MSM simulation clearly exhibits a separation bubble.

To quantitatively assess the effects of mesh resolution and SGS model on predicting the mean separation bubble size, figure 7 shows the mean horizontal length $(L_{\rm s}/L)$ of the predicted separation bubble as a function of the characteristic mesh resolution $(\Delta_{\rm c}/L)$. For reference, the corresponding DNS data (Uzun & Malik 2022) is also included, where the mean horizontal length of the separation bubble is approximately 0.32L. The variations in separation bubble length with mesh resolution show a complex trend. For the SM simulations, convergence with mesh refinement is non-monotonic, producing a spurious reduction of the separation bubble upon as the mesh is refined. Such non-monotonic convergence toward DNS or experimental results has also been reported in previous studies with various isotropic SGS models and wall models (Whitmore *et al.* 2021; Agrawal *et al.* 2022; Zhou & Bae 2024a), supporting the view that this behavior stems from limitations in the SGS model.

In contrast, the MSM predicts a larger separation bubble but yields results that are consistent across mesh resolutions, suggesting that including an anisotropic SGS stress term provides a beneficial effect. Similar consistency in separation-bubble prediction has

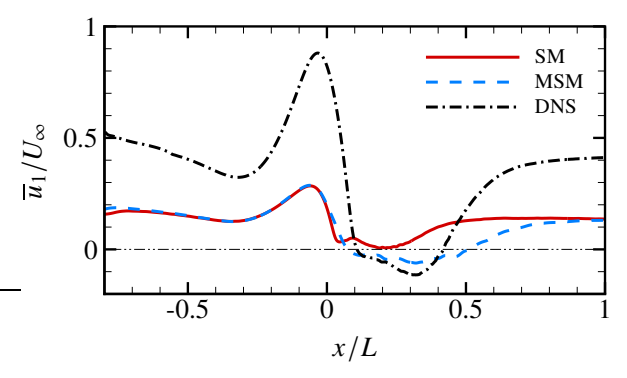


Figure 6: Mean streamwise velocity at the first off-wall cell center from the medium-mesh simulations with the SM and MSM, and the reference DNS results (Uzun & Malik 2022) at the same wall-normal location. $\overline{u}_1 = 0$ is indicated by the horizontal line.

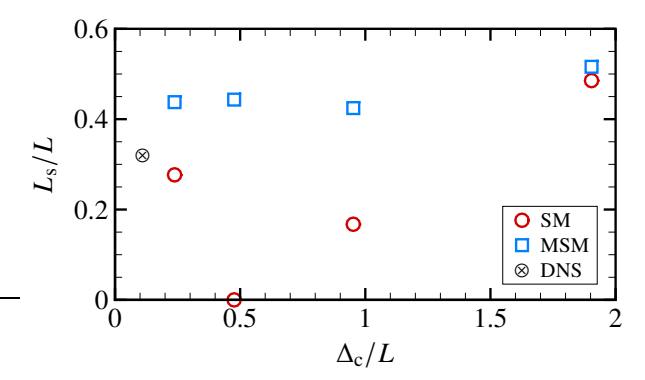


Figure 7: Mean separation bubble length on the leeward side of the bump from the simulations using the SM and MSM for different mesh resolutions and the reference DNS (Uzun & Malik 2022). Symbols represent data point for each case.

also been observed with the mixed model (Bardina 1983; Sarghini *et al.* 1999), as discussed in §B and (Zhou & Bae 2024*a*). Since the current MSM has not been optimized and employs a fixed Smagorinsky coefficient, further improvement may be acheived through dynamic coefficients or other optimization strategies.

As the mesh is refined to the fine-mesh resolution, results from all simulations converge and approach the DNS data. This fine mesh achieves a resolution close to WRLES, particularly within the separation bubble, where the boundary layer thickness is resolved by more than 150 cells. Under such resolution, the dependence of the mean flow prediction on the SGS model is significantly reduced.

The results presented in this section highlight the sensitivity of the predicted mean velocity field in WMLES to both the SGS model and mesh resolution, consistent with observations from previous studies (Rezaeiravesh *et al.* 2019; Lozano-Durán & Bae 2019; Whitmore *et al.* 2020; Iyer & Malik 2022; Zhou & Bae 2024*a*). Because the mean velocity is one of the most important first-order statistical quantities that WMLES aims to predict, understanding the underlying mechanisms behind the sensitivity is essential. This leads to two key questions. First, why does the predicted mean velocity on the leeward side of the bump differ qualitatively between simulations using isotropic and anisotropic SGS models, particularly at medium mesh resolution? Second, why do simulations employing anisotropic SGS models yield more

consistent predictions of the mean separation bubble size across different mesh resolutions compared with isotropic SGS models? To answer these questions, a series of analyses are conducted, as detailed in the following sections.

3.2. Identification of the critical region for SGS anisotropy effect

According to the aforementioned results, the prediction of the separation bubble is strongly influenced by the choice of SGS model. In particular, compared with the SM, the MSM provides more consistent and accurate predictions of the separation bubble on the leeward side of the bump, underscoring the importance of SGS anisotropy. To better understand the role of anisotropic SGS stress in the mean flow field and in the formation of the separation bubble, a numerical experiment is designed to identify where the anisotropy effects becomes most critical. In this experiment, a series of LES are performed using the same computational domain as before and the previously defined medium mesh. However, the domain is divided into upstream and downstream sections, as illustrated in figure 8. In each section, a different SGS model is employed. At the virtual interface between the two sections, a logistic function is used to smoothly transition from one SGS model to another. All simulations use the same boundary conditions as before.

Regarding the SGS models, the classical SM and the MSM discussed earlier are selectively assigned to the two domain sections. Based on previous studies of flow over a Gaussian bump (Uzun & Malik 2022; Prakash $et\ al.\ 2024$; Xu & Bermejo-Moreno 2024), the flow near the bump peak plays an important role in the formation of the downstream separation bubble. Therefore, in this experiment, five different locations of the virtual interface within this region are considered. The details of the interface locations and the selected SGS models for each case are listed in Table 2. In the first group SM-MSM, the upstream section of the domain employs the SM and the downstream section uses the MSM, while in the second group MSM-SM, the upstream section employs the MSM and the downstream section uses the SM. The virtual interface dividing the domain is aligned with the local normal direction of the bump surface, and the x coordinate of its intersection with the bump surface is defined as the interface location, x_0 . Based on this setup, the SGS stress is given by

$$\tau_{ij}^{\rm sgs} = \tau_{ij}^{\rm iso} + g \cdot \tau_{ij}^{\rm ani} = \tau_{ij}^{\rm SM} + g \cdot \tau_{ij}^{\rm ani} \ . \eqno(3.1)$$

Here, g is a logistic function used to achieve a smooth transition from one SGS model to another in the computational domain, and its form for the two groups of simulations is given by

$$g = \begin{cases} \frac{g_0}{1 + e^{k \times d \times \varphi}} & \text{(SM-MSM)} \\ \frac{g_0}{1 + e^{-k \times d \times \varphi}} & \text{(MSM-SM)} \end{cases},$$
(3.2)

where $g_0 = 1$, d is the spatial distance from a point in the domain to the virtual interface at x_0 , and k controls the effective width of the interface. In the present setup, k = 5000, giving an approximate effective width of $5 \times 10^{-3} L$, which corresponds to ten cells in the medium mesh. Tests with interface widths ranging from $1 \times 10^{-3} L$ to $1 \times 10^{-2} L$ showed no significant influence on the resulting mean velocity fields. The parameter φ is equal to 1 upstream of the centerline of the interface and -1 downstream of it. Moreover, for each simulation in the experiment, the first two flow-through times are discarded to remove initial transients, and flow statistics are collected over the following three flow-through times.

Figure 9 shows the predicted mean separation bubble size (L_s/L) , as well as the location of the mean separation point (x_s/L) from the simulations in the experiment. The results indicate that when the interface is placed at the most upstream location $(x_0/L = -0.3)$, the

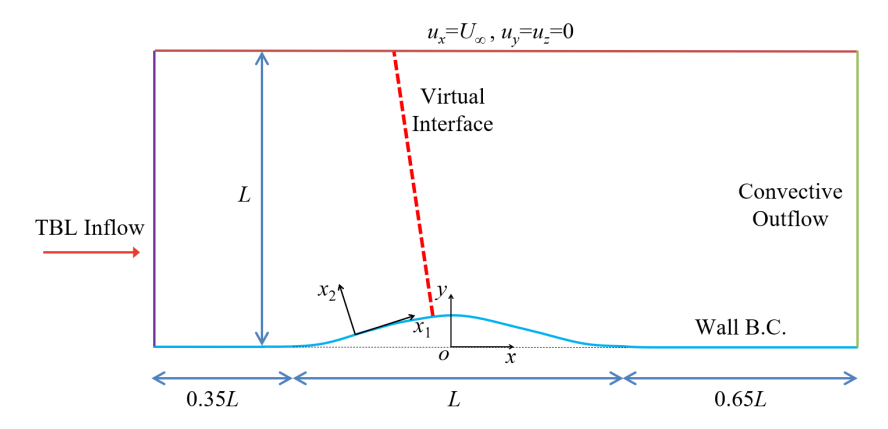


Figure 8: Virtual-interface setup dividing the domain into upstream and downstream regions using different SGS models for the flow over a Gaussian bump.

Group index	Virtual interface location x_0/L	SGS models in the upstream / downstream
SM-MSM	-0.3 -0.2	SM / MSM
MSM-SM	-0.1 0.0 0.05	MSM / SM

Table 2: List of parameters for the virtual interface setup.

predictions are similar to those from the simulation using only the SGS model applied in the downstream section over the entire domain. As the interface is shifted downstream, the predictions become increasingly similar to those obtained using the SGS model applied in the upstream section over the entire domain. For example, in the cases of the group SM-MSM, when the interface is located at $x_0/L = -0.3$, the predicted downstream separation bubble closely matches that from the simulation with the MSM over the entire domain, for which the separation bubble size reaches 0.44L. As the interface is shifted downstream, the separation bubble on the leeward side of the bump gradually decreases in size. When the interface reaches the leeward side of the bump $(x_0/L = 0.05)$, the separation bubble disappears, and the flow field becomes similar to that of the simulation with the SM applied over the entire domain. An opposite trend is observed for the cases of the group MSM-SM. The most pronounced variations occur as the interface moves from $x_0/L = -0.2$ to the bump peak, where the FPG remains strong. Beyond the bump peak, shifting the interface farther downstream has a smaller influence, and the predicted separation bubble remains nearly unchanged.

To examine how the TBL changes with the variation of the virtual interface locations within the critical FPG region $(x \in [-0.2, 0])$, the velocity statistics at the bump peak (x/L = 0) are analyzed. In addition to the mean streamwise velocity \overline{u}_1 , the Reynolds shear stress $\overline{u'_1u'_2}$ and the wall-normal Reynolds normal stress $\overline{u'_2u'_2}$ are examined, since these stresses play important roles in shaping the near-wall mean flow, as will be illustrated later in §4.1 and §4.3. The results from the two groups of simulations are shown in figures 10 and 11. The comparison again demonstrate that as the interface is shifted downstream, the

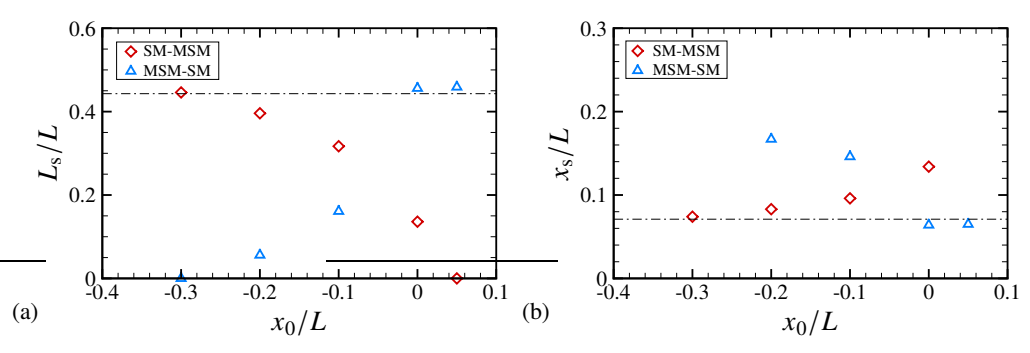


Figure 9: Mean separation bubble length on the leeward side of the bump (a) and the location of mean separation point (b) from medium-mesh simulations using the SM-MSM and MSM-SM with different virtual interface locations. Horizontal lines indicate the results from the medium-mesh simulation with MSM.

results gradually approach those obtained using the SGS model applied in the upstream section throughout the domain. Furthermore, the DNS data exhibit pronounced internal peaks in the profiles of Reynolds stresses at this location. According to the investigation from Uzun & Malik (2022), these internal peaks play a crucial role in determining the downstream evolution of the TBL and the onset of flow separation on the leeward side. Compared with the DNS, the WMLES predictions of the Reynolds stresses deviate to different degrees, which could be attributed to the use of constant, non-optimized model coefficients in these SGS models. Moreover, as will be discussed in §4.1 and §4.3, it is the wall-normal gradients of the Reynolds stresses, rather than their magnitudes, that more directly influence momentum transport and mean pressure distribution. From the comparisons among the simulations, it is found that applying the MSM within the critical FPG region on the windward side improves the capture of the internal peaks in the Reynolds stress profiles at the bump peak. These results suggest that the predicted size of the separation bubble on the leeward side is strongly influenced by the SGS model used in the upstream region where the FPG is strong. In particular, the ability of the SGS model to reproduce the near-wall trends of the Reynolds stress internal peaks appears to have an important effect on the downstream separation behavior. This finding is consistent with the DNS observations of Uzun & Malik (2022) and will be further examined in the following sections. Overall, the results of this designed numerical experiment highlight that the effect of anisotropic SGS stress on the windward side of the bump is critical. Applying an anisotropic SGS model in the region of strong FPG alters the wall-normal distributions of Reynolds stress and subsequently affects the downstream flow separation.

4. Budget analyses

In this section, we first study the mean streamwise momentum and pressure equations slightly upstream of the mean separation point to isolate the effects of the individual budget terms. We demonstrate that the Reynolds stresses, particularly $\overline{u_1'u_2'}$ and $\overline{u_2'u_2'}$, have a significant impact on the mean flow field. We then analyze the Reynolds stress transport equations to understand how the distributions within the TBL are influenced by anisotropic SGS stress.

This analysis considers the original simulations with the SM and the MSM applied over the entire computational domain. These SGS models nominally share the same kinetic energy dissipation mechanism but differ in their treatment of anisotropic SGS stress. Only the medium mesh simulations are analyzed in §4.1-4.3, as this resolution shows the most

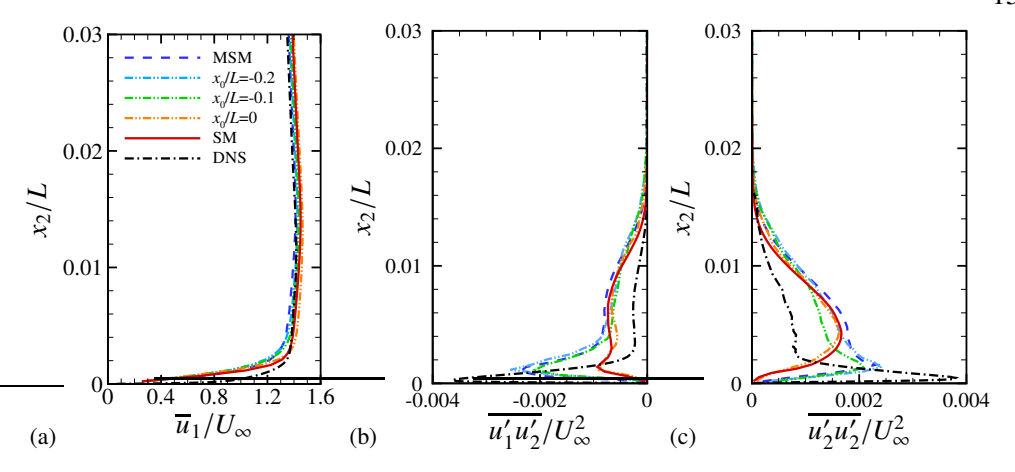


Figure 10: Mean streamwise velocity \overline{u}_1 (a), Reynolds shear stress $\overline{u'_1u'_2}$ (b), and Reynolds normal stress $\overline{u'_2u'_2}$ (c) profiles at the bump peak (x/L=0) for SM-MSM with the virtual interface located at $x_0/L=-0.2, -0.1$, and 0. DNS (Uzun & Malik 2022), SM and MSM results are shown for reference.

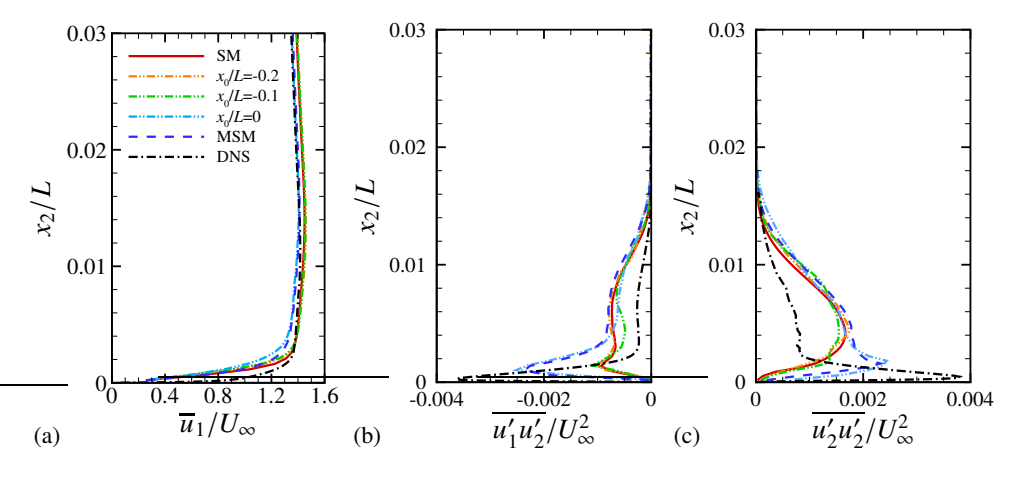


Figure 11: Mean streamwise velocity $\overline{u_1}$ (a), Reynolds shear stress $\overline{u_1'u_2'}$ (b), and Reynolds normal stress $\overline{u_2'u_2'}$ (c) profiles at the bump peak (x/L=0) for MSM–SM with the virtual interface located at $x_0/L=-0.2, -0.1$, and 0. DNS (Uzun & Malik 2022), SM and MSM results are shown for reference.

pronounced differences in separation bubble prediction between the two models (see figure 7). We then study the effect of mesh resolution on the separation bubble prediction in §4.4. The analysis aims to address why the predicted flow on the leeward side of the bump differs qualitatively between the simulations using these two SGS models.

4.1. Mean streamwise momentum

Considering the homogeneity of the current statistically stationary flow in the spanwise direction, the streamwise mean momentum equation can be expressed as

$$\overline{u}_1 \frac{\partial \overline{u}_1}{\partial x_1} + \overline{u}_2 \frac{\partial \overline{u}_1}{\partial x_2} = P_g + V_{11} + V_{12} + T_{11} + T_{12} + R_{11} + R_{12} , \qquad (4.1)$$

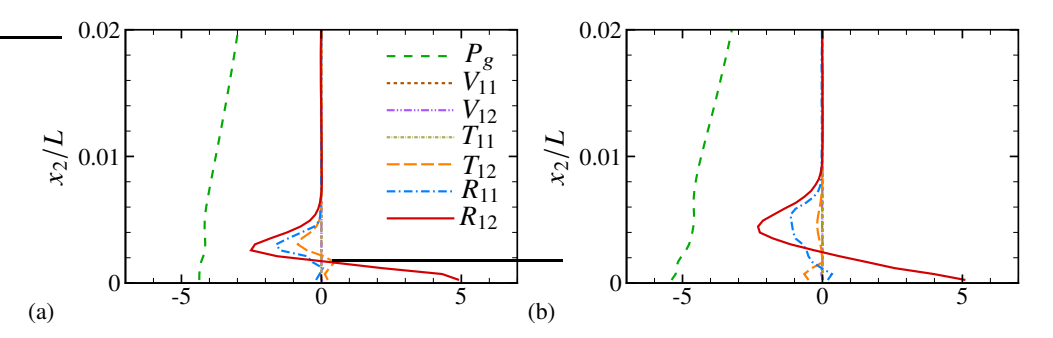


Figure 12: Mean streamwise momentum budget terms at x/L = 0.05 from medium-mesh simulations with the SM (a) and MSM (b). All terms are nondimensionalized using U_{∞} , L and ρ . The line notations correspond to equations (4.2)–(4.4).

where the seven terms on the right-hand side of the equation are

$$P_g = -\frac{1}{\rho} \frac{\partial \overline{p}}{\partial x_1}, \qquad V_{11} = \frac{\partial}{\partial x_1} \left(2\nu \overline{S}_{11} \right), \qquad V_{12} = \frac{\partial}{\partial x_2} \left(2\nu \overline{S}_{12} \right), \tag{4.2}$$

$$T_{11} = \frac{\partial}{\partial x_1} \left(-\overline{\tau_{11}^{\text{sgs}}} \right), \qquad T_{12} = \frac{\partial}{\partial x_2} \left(-\overline{\tau_{12}^{\text{sgs}}} \right),$$
 (4.3)

$$R_{11} = \frac{\partial}{\partial x_1} \left(-\overline{u_1' u_1'} \right), \qquad R_{12} = \frac{\partial}{\partial x_2} \left(-\overline{u_1' u_2'} \right). \tag{4.4}$$

Specifically, P_g corresponds to the contribution from the mean pressure gradient. V_{11} and V_{12} denote contributions from viscosity. T_{11} and T_{12} represent contributions from the mean SGS stress. The last two terms, R_{11} and R_{12} , denote contributions from the Reynolds stress. The magnitudes of these terms influence the distribution of mean momentum and, consequently, the mean velocity field. It should be noted that curvature effects are neglected in the derivation of the mean momentum equation, since their influence in the region upstream of the mean separation point, where x/L < 0.1, is negligible. The corresponding investigation is described in §A.

Figure 12 shows the mean streamwise momentum budget at x/L = 0.05, approximately one boundary-layer thickness upstream of the separation point in the MSM simulation. The same location is used for the SM case for consistency. Although both simulations exhibit the same dominant balance, the adverse pressure-gradient term, P_g , and the Reynolds shear-stress gradient term, R_{12} , differ quantitatively in ways that directly influence the downstream separation.

In both cases, P_g is strongly negative across the boundary layer, reflecting the strong APG. However, the MSM produces a noticeably larger magnitude of P_g , indicating stronger deceleration of the mean flow. The distributions of R_{12} also differ in a manner essential to the separation mechanism. While the peak magnitude of R_{12} is similar between the two simulations, the MSM exhibits a significantly broader region over which R_{12} is negative. This extended negative region implies that momentum is extracted over a thicker portion of the boundary layer and redistributed toward the near-wall region. Consequently, less streamwise momentum remains available farther from the wall to resist the APG, making the near-wall mean flow more susceptible to decelerating to zero and initiating separation in the MSM case. In contrast, the SM confines the momentum deficit to a thinner layer, helping the flow remain attached despite the strong APG.

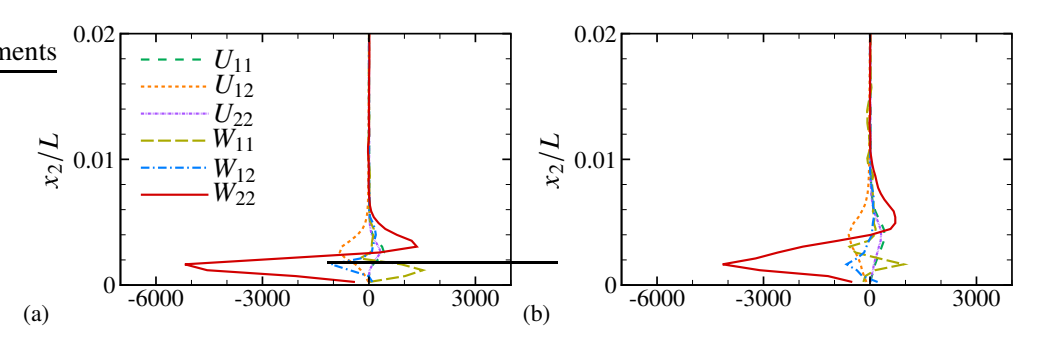


Figure 13: Mean pressure budget terms at x/L = 0.05 from medium-mesh simulations with the SM (a) and MSM (b). All terms are nondimensionalized using U_{∞} , L and ρ . The line notations correspond to equations (4.6) and (4.7).

4.2. Mean pressure equation

The Poisson equation for the mean pressure of the flow is given by

$$-\frac{1}{\rho}\nabla^{2}\overline{p} = \frac{\partial\overline{u}_{i}}{\partial x_{j}}\frac{\partial\overline{u}_{j}}{\partial x_{i}} + \frac{\partial^{2}\overline{u'_{i}u'_{j}}}{\partial x_{i}\partial x_{j}}$$

$$= U_{11} + U_{12} + U_{22} + W_{11} + W_{12} + W_{22} ,$$

$$(4.5)$$

where the six terms on the right-hand side of the equation are

$$U_{11} = \left(\frac{\partial \overline{u}_1}{\partial x_1}\right)^2, \qquad U_{12} = 2\left(\frac{\partial \overline{u}_1}{\partial x_2}\frac{\partial \overline{u}_2}{\partial x_1}\right), \qquad U_{22} = \left(\frac{\partial \overline{u}_2}{\partial x_2}\right)^2,$$
 (4.6)

$$W_{11} = \frac{\partial^2 \overline{u_1' u_1'}}{\partial x_1^2}, \qquad W_{12} = 2 \frac{\partial^2 \overline{u_1' u_2'}}{\partial x_1 \partial x_2}, \qquad W_{22} = \frac{\partial^2 \overline{u_2' u_2'}}{\partial x_2^2}.$$
 (4.7)

The three terms in equation (4.6) represent the contributions from the mean velocity field to the mean pressure, and the remaining three terms in equation (4.7) account for the contributions from the Reynolds stresses.

Figure 13 shows the profiles of all six terms in the mean pressure equation at the streamwise location x/L = 0.05. The results are qualitatively similar for the two simulations with different SGS models. Within the TBL, the term that has the dominant effect on the mean pressure field is W_{22} , which is associated with the wall-normal Reynolds normal stress, $\overline{u_2'u_2'}$. This indicates that variations in the wall-normal turbulent fluctuations are the primary contributors to the local mean pressure distribution.

Taken together with the momentum budget analysis, these results highlight a consistent picture: in the medium-mesh simulations, the Reynolds stresses, not the mean SGS stresses, govern both the mean velocity and mean pressure fields immediately upstream of the separation point. Although the two SGS models produce different downstream separation behavior, those differences arise primarily from how each model shapes the Reynolds-stress distributions within the upstream FPG region. The mean SGS stresses, by comparison, make only a minor contribution at this location.

4.3. Reynolds stress transport equation

Based on the mean momentum and pressure budget analyses, we examine the Reynolds shear stress $\overline{u_1'u_2'}$ and the Reynolds normal stress $\overline{u_2'u_2'}$ at three streamwise locations within the FPG region upstream of the bump peak. Figure 14 shows the wall-normal profiles of

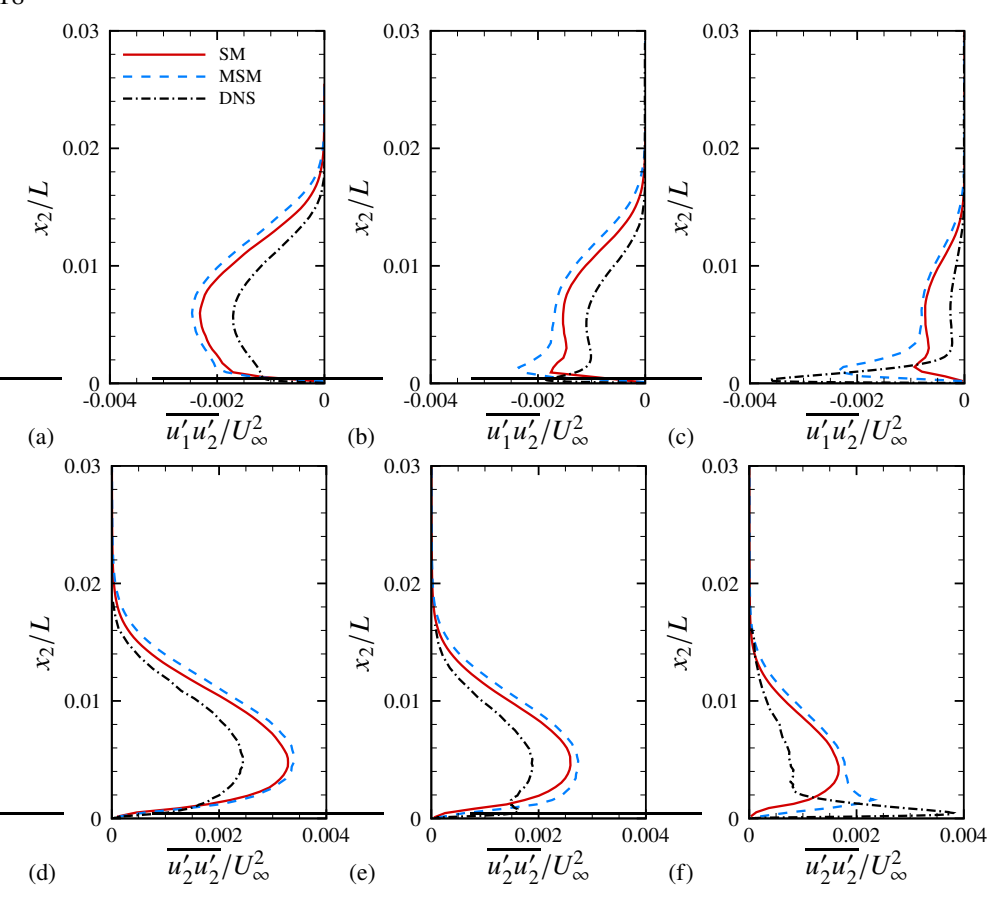


Figure 14: Reynolds shear stress $\overline{u_1'u_2'}$ (a-c) and Reynolds normal stress $\overline{u_2'u_2'}$ (d-f) profiles at x/L = -0.2 (a,d), x/L = -0.1 (b,e), and x/L = 0 (c,f) for SM, MSM and reference DNS (Uzun & Malik 2022).

the Reynolds stresses from the two medium-mesh simulations, along with DNS results from Uzun & Malik (2022) for reference.

The DNS data indicate that, along the streamwise direction, the magnitudes of the Reynolds shear and normal stresses gradually increase in the near-wall region and exhibit a distinct internal peak in the FPG region. Both medium-mesh simulations deviate noticeably from the DNS data, with both overpredicting Reynolds stresses in the outer layer. It should be mentioned that the SGS models in these simulations use constant model coefficients and have not been optimized for WMLES of this flow configuration. The most prominent distinction between the two simulations is that the MSM reproduces clear internal peaks of $\overline{u_1'u_2'}$ and $\overline{u_2'u_2'}$ at $x_2/L \approx 1.3 \times 10^{-3}$, slightly above the DNS location, while the SM does not capture these features. This upward shift of the internal peaks in the MSM case is partly due to the coarse mesh resolution in the present WMLES.

As shown in §4.1, the wall-normal gradient of $\overline{u_1'u_2'}$ is closely related to mean momentum transport, while the gradient of $\overline{u_2'u_2'}$ is associated with the mean pressure distribution. Therefore, accurately capturing the wall-normal variation of these stresses, which determines the sign and magnitudes of these gradients, is essential for predicting downstream flow separation. The improved prediction of Reynolds stress profiles in the MSM simulation,

particularly the internal stress peak under FPG conditions, demonstrates the benefit of incorporating anisotropic SGS stress. As discussed by Uzun & Malik (2022), these internal peaks evolve downstream and strongly influence the mean flow and separation onset. This is consistent with the present as well as the earlier analysis in §3.2. Taken together, the results indicate that the improved prediction of flow separation in the MSM simulation is linked to its ability to better reproduce Reynolds stress distributions, particularly the internal peak in the FPG region. This improvement is closely associated with changes in downstream Reynolds stresses, the mean velocity field, and ultimately the separation bubble development.

To better understand the impact of the SGS model on the Reynolds shear stress $\overline{u_1'u_2'}$ and the Reynolds normal stress $\overline{u_2'u_2'}$, it is necessary to analyze the Reynolds stress transport equation, with particular attention to the individual contributions from the SGS model. Based on the Reynolds decomposition and the assumption of homogeneity in the spanwise direction, the transport equation for the resolved Reynolds stresses in LES can be expressed as

$$\frac{\partial \overline{u_i'u_j'}}{\partial t} + \overline{u}_k \frac{\partial \overline{u_i'u_j'}}{\partial x_k} = P_{ij} - \varepsilon_{ij} + \phi_{ij} + \xi_{ij} + \frac{\partial}{\partial x_k} \left(\zeta_{ijk} + D_{ijk} + T_{ijk} + J_{ijk} \right), \quad (4.8)$$

where

$$P_{ij} = -\overline{u'_i u'_k} \frac{\partial \overline{u}_j}{\partial x_k} - \overline{u'_j u'_k} \frac{\partial \overline{u}_i}{\partial x_k} , \qquad (4.9)$$

$$\varepsilon_{ij} = 2\nu \overline{\left(S'_{ik} \frac{\partial u'_{j}}{\partial x_{k}} + S'_{jk} \frac{\partial u'_{i}}{\partial x_{k}}\right)} = 2\nu \overline{\left(\frac{\partial u'_{i}}{\partial x_{k}} \frac{\partial u'_{j}}{\partial x_{k}}\right)}, \tag{4.10}$$

$$\phi_{ij} = \frac{\overline{p'}}{\rho} \cdot \left(\frac{\partial u'_i}{\partial x_j} + \frac{\partial u'_j}{\partial x_i} \right) = 2 \frac{\overline{p'}}{\rho} S'_{ij} , \qquad (4.11)$$

$$\xi_{ij} = \overline{(\tau_{ik}^{\text{sgs}})' \frac{\partial u'_j}{\partial x_k} + (\tau_{jk}^{\text{sgs}})' \frac{\partial u'_i}{\partial x_k}}, \qquad (4.12)$$

$$\frac{\partial}{\partial x_k} \zeta_{ijk} = -\frac{\partial}{\partial x_k} \left[\overline{(\tau_{ik}^{\text{sgs}})' u_j'} + \overline{(\tau_{jk}^{\text{sgs}})' u_i'} \right] , \qquad (4.13)$$

$$\frac{\partial}{\partial x_k} D_{ijk} = \nu \frac{\partial^2 \overline{u_i' u_j'}}{\partial x_k^2} = 2\nu \frac{\partial}{\partial x_k} \left(\overline{S_{ik}' u_j'} + \overline{S_{jk}' u_i'} \right) , \qquad (4.14)$$

$$\frac{\partial}{\partial x_k} T_{ijk} = -\frac{\partial}{\partial x_k} \overline{u_i' u_j' u_k'}, \qquad (4.15)$$

$$\frac{\partial}{\partial x_k} J_{ijk} = -\frac{\partial}{\partial x_k} \left(\overline{p'u_i'} \delta_{jk} + \overline{p'u_j'} \delta_{ik} \right) . \tag{4.16}$$

The terms given in equations (4.9)–4.16 correspond to production, viscous dissipation, pressure strain, SGS dissipation, SGS diffusion, viscous diffusion, turbulent diffusion, and pressure diffusion, respectively. In particular, the terms expressed in equations (4.12) and 4.13 are associated with SGS stress fluctuations and directly represent the contributions from the SGS model. While the magnitudes of these terms in the Reynolds-stress transport equations are generally smaller than leading-order contributions such as production and pressure redistribution in the near-wall region, they remain physically meaningful and can be influential. The SGS dissipation represents the local transfer of resolved-scale energy to

unresolved scales, whereas the SGS diffusion corresponds to the spatial redistribution of energy. Their importance also lies in how they modulate the expression of other budget terms in the resolved flow, thereby influencing the overall distribution of Reynolds stresses.

Figure 15 shows the comparison of SGS dissipation and SGS diffusion from the mediummesh simulations with the SM and the MSM at the three streamwise locations discussed above. The wall-normal range in each plot focuses on the near-wall region of the boundary layer, where the effects of SGS dissipation and diffusion are most pronounced. The SGS dissipation results indicate that the SM and MSM produce qualitatively different behaviors for both $\overline{u_1'u_2'}$ and $\overline{u_2'u_2'}$. In the SM, the SGS dissipation remains positive for $\overline{u_1'u_2'}$ and negative for $\overline{u_2'u_2'}$, showing that the SGS stress fluctuations consistently act as a sink of Reynolds stresses, with a net removal of resolved energy into the SGS scales. In contrast, the MSM yields negative SGS dissipation for $\overline{u_1'u_2'}$ in the inner layer and positive values for $\overline{u_2'u_2'}$ in the very near-wall region. This behavior indicates that the SGS stress fluctuations in the MSM can produce a net backscatter of energy, transferring it from unresolved to resolved scales and locally enhancing the Reynolds stresses. This backscatter effect is physically significant. On a coarse mesh, the cutoff lies in the energy-containing range or in the energetic part of the inertial range, so the unresolved motions carry a substantial fraction of turbulent energy and momentum fluxes. Consequently, the SGS stress must not only remove resolved energy but also be capable of returning energy into the resolved field. Moreover, in the near-wall region, turbulence is highly anisotropic and the near-wall cycle involves essential small-scale dynamics. These mechanisms become even more crucial in TBLs with pressure gradients, such as in the present case. A coarse-mesh LES that does not capture these near-wall scales omits an important pathway by which energy is both removed from and supplied back to the larger scales.

The SGS diffusion results for both $\overline{u_1'u_2'}$ and $\overline{u_2'u_2'}$ reveal important differences between the SM and MSM. For the Reynolds shear stress $\overline{u_1'u_2'}$, the SM produces negative SGS diffusion very close to the wall, which then becomes positive away from the wall before eventually decaying to zero. In contrast, the MSM yields negative SGS diffusion throughout the near-wall region, monotonically approaching zero with wall-normal distance. Since SGS diffusion represents movement of Reynolds stresses by unresolved motions, with negative values indicating movement into a location and positive values indicating movement away, the positive region in the SM profile implies that SGS motions redistribute $\overline{u_1'u_2'}$ away from the near wall region to parts where the SGS diffusion is negative. The MSM, however, continuously moves $\overline{u_1'u_2'}$ toward the near-wall region.

For the Reynolds normal stress $\overline{u_2'u_2'}$, the SM gives positive SGS diffusion near the wall, decreasing with distance, becoming slightly negative, and then approaching zero. The MSM, by contrast, shows negative diffusion very close to the wall, positive values near the internal peak of $\overline{u_2'u_2'}$, and negative values again farther out. This pattern indicates that the MSM moves $\overline{u_2'u_2'}$ into the internal-peak region from both sides, while the SM primarily redistributes it from the outer region toward the wall.

These SGS diffusion behaviors, combined with the differences in SGS dissipation, help explain why the MSM produces the internal Reynolds-stress peaks observed in figure 14, whereas the SM does not.

As described in §2, the MSM expresses the SGS stress $\tau_{ij}^{\rm sgs}$ as equation (2.4), which contains the isotropic stress term $\tau_{ij}^{\rm iso}$ from the SM and an additional anisotropic term $\tau_{ij}^{\rm ani}$. To clarify their roles, the individual contributions from them are analyzed separately. Figure 16 shows the wall-normal distributions of SGS dissipation and diffusion in the medium-mesh

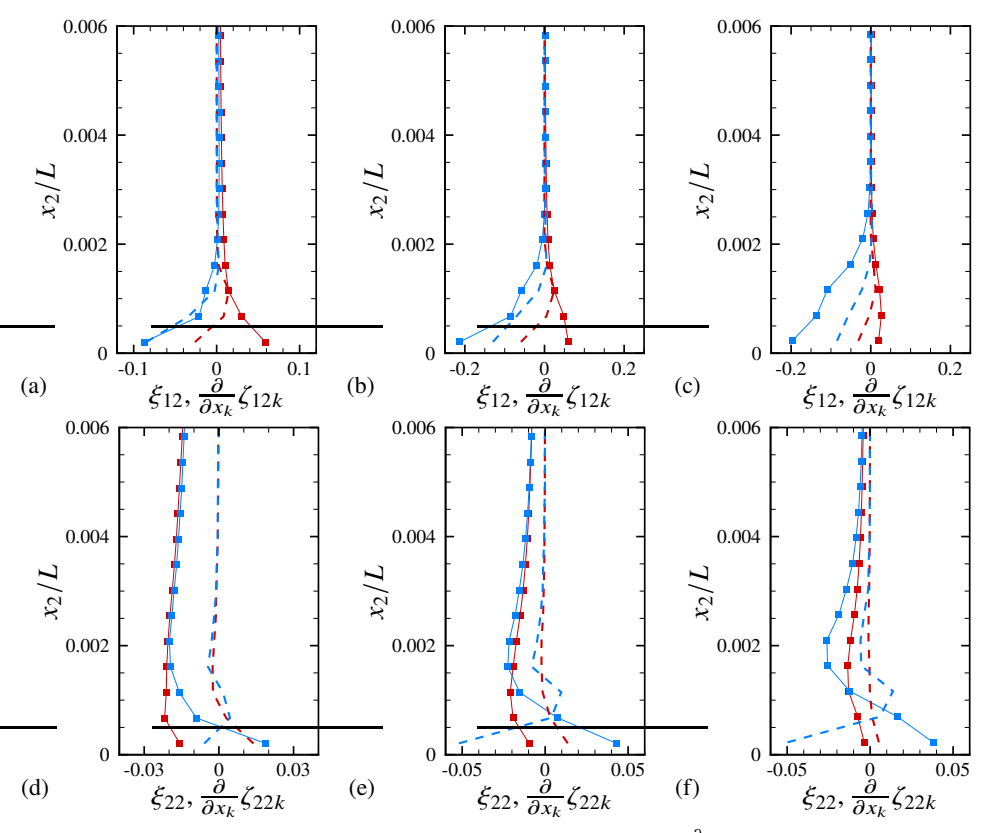


Figure 15: SGS dissipation ξ_{ij} (solid square) and diffusion $\frac{\partial}{\partial x_k}\zeta_{ijk}$ (dashed) for the Reynolds shear stress $\overline{u_1'u_2'}$ (a–c) and the wall-normal Reynolds normal stress $\overline{u_2'u_2'}$ (d–f) at x/L=-0.2 (a,d), x/L=-0.1 (b,e), and x/L=0 (c,f) for SM (red) and MSM (blue) simulations on the medium-mesh. All terms are nondimensionalized using U_∞ , L and ρ .

simulation with the MSM. For the SGS dissipation associated with both the Reynolds shear stress $\overline{u_1'u_2'}$ and the Reynolds normal stress $\overline{u_2'u_2'}$, the contribution of the isotropic stress term behaves similarly to the SM that shown in figure 15. It consistently acts as a sink of resolved energy, with a magnitude larger than in the SM alone. In contrast, the contribution of the anisotropic stress term generates significant local production in the near-wall inner layer. This indicates that SGS anisotropy is the primary source of backscatter in the MSM, transferring energy from unresolved to resolved scales and enhancing the Reynolds stresses. For the SGS diffusion associated with Reynolds shear stress, the contribution of isotropic stress term again resembles the SM. It is negative very close to the wall, becomes positive away from the wall, and decays toward zero, reflecting a wall-normal redistribution of $\overline{u_1'u_2'}$ from locations with positive diffusion toward locations with negative diffusion. The contribution of anisotropic stress term shows the opposite pattern, with negative values near $x_2/L \approx 1.3 \times 10^{-3}$, which is the wall-normal location of the internal shear-stress peak. For the SGS diffusion of the Reynolds normal stress, the isotropic part redistributes energy from the outer region toward the very near-wall region, while the anisotropic part redistributes energy into the internalpeak location from its neighboring wall-normal regions. Taken together, the dissipation and diffusion decompositions indicate that the anisotropic SGS stress in the MSM is responsible for the redistribution of energy toward the wall-normal locations around the internal peak of the Reynolds stresses.

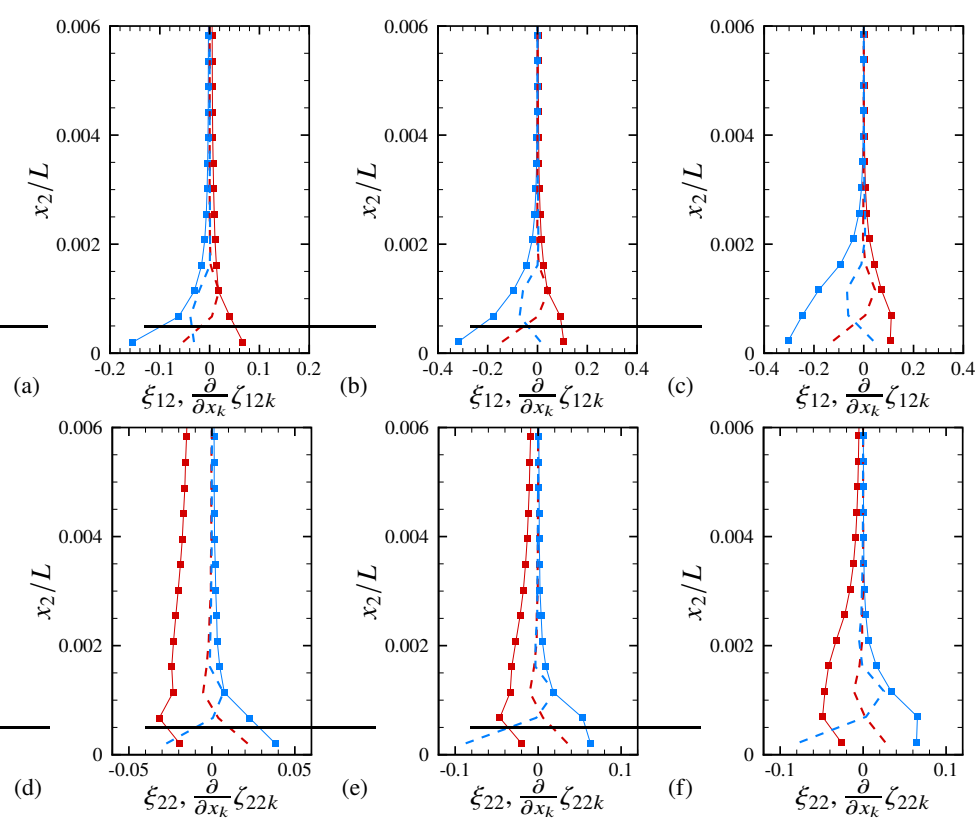


Figure 16: SGS dissipation ξ_{ij} (solid square) and diffusion $\frac{\partial}{\partial x_k} \zeta_{ijk}$ (dashed) from the isotropic (red) and anisotropic (blue) stress components of the MSM for the Reynolds shear stress $u_1'u_2'$ (a–c) and the wall-normal Reynolds normal stress $u_2'u_2'$ (d–f) at x/L = -0.2 (a,d), x/L = -0.1 (b,e), and x/L = 0 (c,f). All terms are nondimensionalized using U_∞ , L and ρ .

The analyses in this section demonstrate that fluctuations of the SGS stress strongly influence the distributions of Reynolds stresses within the critical FPG region. In this region, the fluctuations of isotropic SGS stress act primarily as a dissipative sink for the Reynolds shear stress $\overline{u'_1u'_2}$ and the wall-normal normal stress $\overline{u'_2u'_2}$. In contrast, the fluctuations of anisotropic SGS stress provide significant backscatter and wall-normal redistribution of energy, which facilitates the formation of the internal peaks of these stresses in the near-wall region of the TBL. This mechanism further impacts the downstream development of the Reynolds stresses and, in turn, alters the mean flow field on the leeward side of the bump, particularly the onset of separation. These results indicate that enabling accurate WMLES predictions requires accurately representing the complex near-wall SGS dynamics, which in turn relies on properly accounting for SGS stress fluctuations in the SGS model.

4.4. Influence of mesh resolution

Through the analysis and comparison of the medium-mesh simulations with isotropic and anisotropic SGS models in the previous sections, we have answered the first question raised in §3, namely why the predicted flow on the leeward side of the bump differs qualitatively between these medium-mesh simulations. The second question, which asks why simulations with anisotropic SGS models provide more consistent predictions of the separation bubble

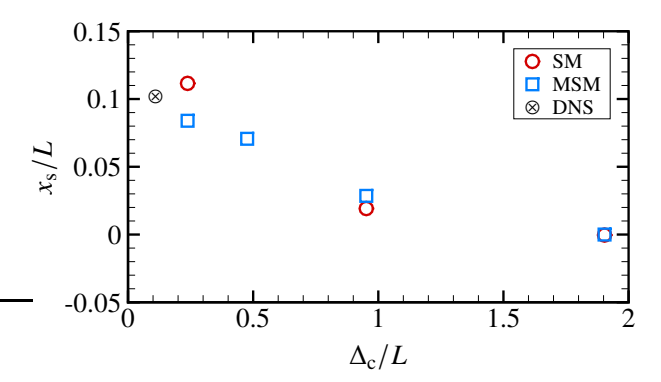


Figure 17: Mean separation point from simulations using the SM and MSM for different mesh resolutions and from the reference DNS (Uzun & Malik 2022). No separation is detected in the medium-mesh simulation ($\Delta_c/L \approx 4.76 \times 10^{-4}$) with the SM.

size across different mesh resolutions compared to those with isotropic SGS models, remains to be addressed. To gain further insight into this question, we analyze the simulation results across different mesh resolutions. In particular, to assess the relative contributions of the mean SGS stress and Reynolds stress to the mean velocity field and the onset of flow separation, we examine the budgets of the mean streamwise momentum equation at a location immediately upstream of the mean separation point, following the same approach as in §4.1.

The predicted mean separation points in the simulations with the SM and the MSM are shown in figure 17. When the coarsest mesh is used, both simulations capture flow separation on the leeward side of the bump. Not only are the predicted mean separation bubble sizes similar (see figure 7), but the predicted mean separation points are also consistent, with their locations close to the bump peak. As the mesh resolution is refined, the mean separation location gradually shifts downstream and the difference between the two simulations becomes larger. In particular, with the medium mesh, the separation bubble disappears in the simulation with the SM. When the mesh is further refined to the fine resolution, both simulations again predict a separation bubble on the leeward side of the bump, and the mean separation point approaches the reference location from the DNS (Uzun & Malik 2022).

In examining the budgets of the mean streamwise momentum equation (equation (2.2)) for each simulation, the analysis is performed at a position 0.02L upstream of the corresponding mean separation point along the x direction, which is approximately one boundary layer thickness upstream of separation. For the medium-mesh simulation with the SM, where no separation bubble forms on the leeward side of the bump, the same location as in the medium-mesh MSM simulation is used for consistency. The results for the SM and MSM simulations are presented in figures 18 and 19, respectively. With the coarsest mesh, both simulations behave qualitatively similarly. The mean SGS shear-stress gradient term T_{12} dominates in the lower half of the TBL, while other terms remain relatively small across the boundary layer. It should be noted that this investigated spatial location lies slightly upstream of the bump peak, where the pressure gradient is close to zero. On the coarse mesh, the predicted mean separation point shifts further downstream in both simulations, and the APG effect becomes stronger, particularly in the MSM case. At the same time, while T_{12} remains important, the contribution of R_{12} increases noticeably within the near-wall region in the MSM simulation. As the resolution increases to the medium mesh, the predicted separation behavior becomes qualitatively different between the two SGS models, as discussed earlier. Compared with coarser meshes, the contribution of T_{12} decreases substantially in both simulations. With the fine mesh, the behavior of the budget terms in the SM and MSM cases

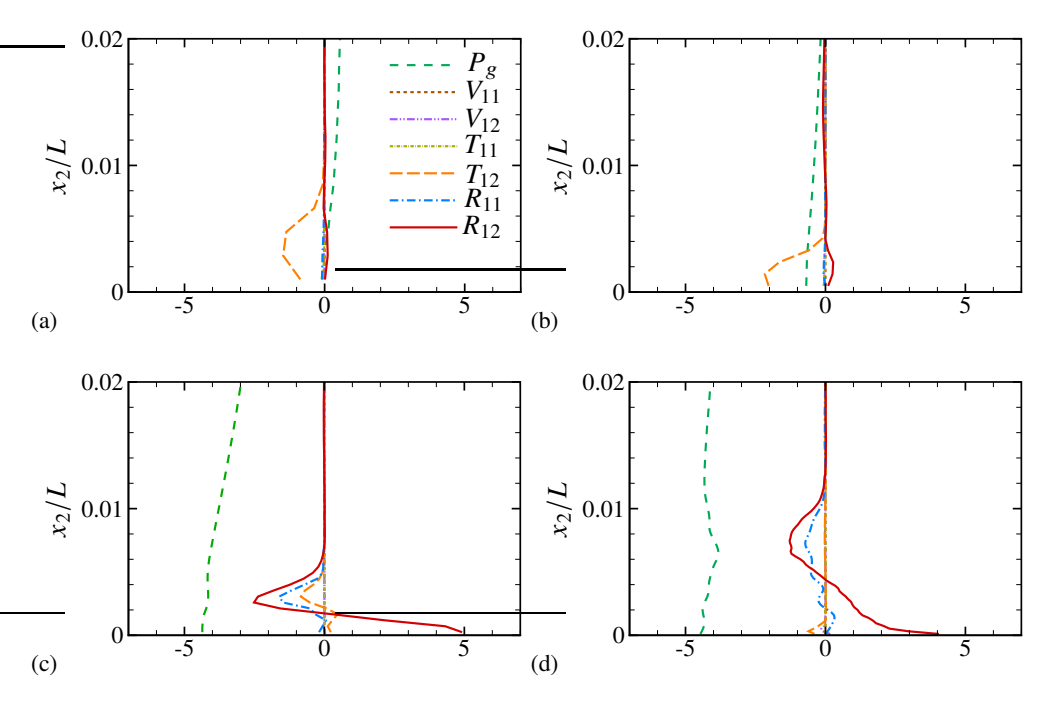


Figure 18: Mean streamwise momentum budget terms at 0.02L upstream of the mean separation point along the x direction from cases with SM for the coarsest mesh (a), coarse mesh (b), medium mesh (c), and fine mesh (d). All terms are nondimensionalized using U_{∞} , L and ρ . The line notations correspond to equations (4.2)–(4.4).

becomes similar again, with R_{12} and P_g emerging as the dominant contributions. Notably, in the SM case, the negative portion of R_{12} extends over a wider wall-normal range than in the medium-mesh SM case. This indicates that momentum is extracted over a thicker layer and redistributed toward the near-wall region where R_{12} is positive. Such redistribution reduces the streamwise momentum available downstream to resist the APG, ultimately leading to mean flow separation in the fine-mesh simulation with the SM. In addition, the contribution of R_{11} , associated with the Reynolds normal stress $\overline{u_1'u_1'}$, also becomes important in both simulations.

These results suggest that in the current WMLES, when coarse grid resolutions such as the coarsest and coarse meshes are used, many flow structures remain unresolved because their scales are smaller than the grid size. Under these conditions, the mean SGS shear stress $\overline{\tau}_{12}^{sgs}$ dominates the mean streamwise momentum balance upstream of the mean separation point, while the contribution from Reynolds stress is relatively small. The difference between the SM and the MSM lies in the anisotropic SGS stress term (see equation (2.4)); however, as will be shown in §5, its contribution to the shear stress component $\overline{\tau}_{12}^{sgs}$ in the near-wall region is limited. Consequently, both models behave similarly in predicting the mean velocity field. When the medium mesh, representative of typical WMLES resolution, is used, more flow scales are resolved. As a result, the importance of the mean SGS shear stress decreases, while Reynolds stresses play a more significant role in the mean momentum transport. As discussed earlier in §4.3, the anisotropic SGS stress term in the MSM modifies the effect of SGS stress fluctuations, which improves the prediction of Reynolds stresses and thereby the prediction of downstream flow separation. For the fine mesh, which has a characteristic resolution similar to typical WRLES, more flow scales are resolved, leaving the SGS model

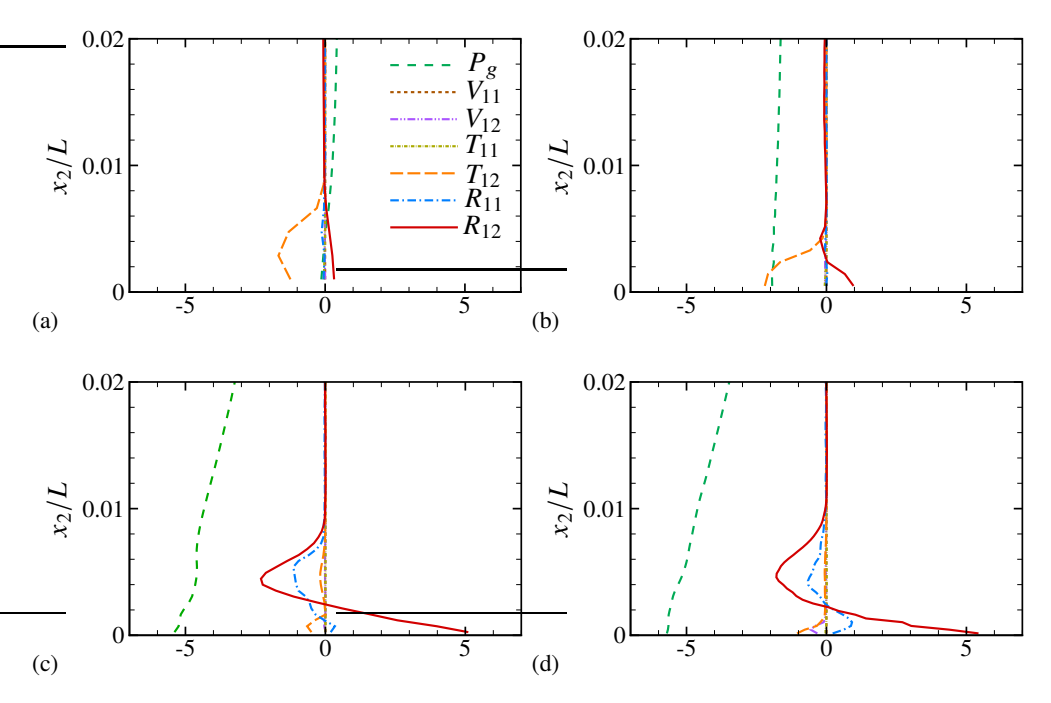


Figure 19: Mean streamwise momentum budget terms at 0.02L upstream of the mean separation point along the x direction from cases with MSM for the coarsest mesh (a), coarse mesh (b), medium mesh (c), and fine mesh (d). All terms are nondimensionalized using U_{∞} , L and ρ . The line notations correspond to equations (4.2)–(4.4).

to account only for the smallest motions. In this case, the influence of the SGS model on both mean velocity and Reynolds stress predictions becomes weaker, and the difference between the SM and MSM results reduces substantially. These findings highlight that, to design a robust SGS model capable of providing accurate predictions of mean flow fields across various mesh resolutions for complex configurations, it is essential to model both the mean SGS stress and the SGS stress fluctuations effectively.

5. Properties of SGS stress

In this section, we examine the properties of the SGS stress and the underlying mechanism of the anisotropic SGS stress. The investigation focuses on the critical FPG region in front of the bump peak, where the anisotropic SGS stress has a strong effect and significantly influences the mean flow separation downstream of the bump peak.

5.1. Mean SGS stress

We first examine the mean SGS stress at x/L = -0.1, located near the center of the critical FPG region where the TBL remains attached in all simulations. Figure 20 shows the wall-normal distributions of the six independent components of the mean SGS stress from the medium-mesh simulations using the SM and MSM. As discussed earlier, the medium mesh exhibits the strongest discrepancy in downstream mean-flow prediction between the two models.

In both simulations, the mean SGS stress is significant only in the very near-wall region, with the dominant component being the shear stress $\overline{\tau_{12}^{\text{sgs}}}$, as expected from the large wall-

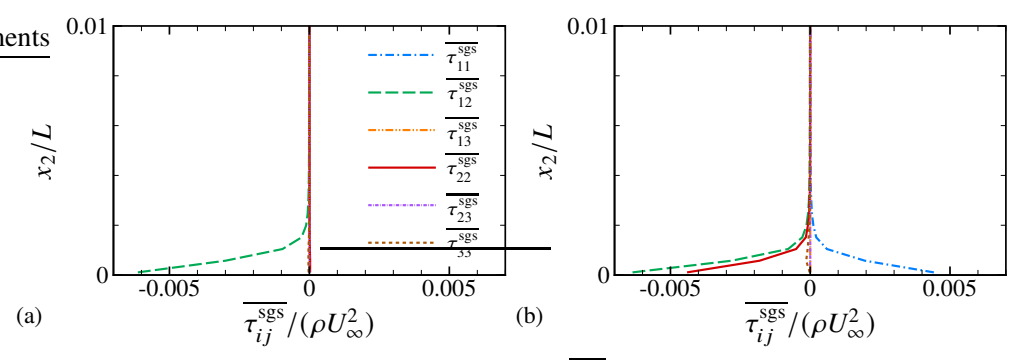


Figure 20: Mean SGS stress tensor components $\overline{\tau_{ij}}^{\text{sgs}}$ at x/L = -0.1 for medium-mesh simulations with the SM (a) and MSM (b).

normal gradient of the streamwise velocity. In the SM case, the remaining components are negligible relative to this dominant shear stress. In contrast, the MSM produces two additional stress components of appreciable magnitude, $\overline{\tau_{11}^{\rm sgs}}$ and $\overline{\tau_{22}^{\rm sgs}}$, which modify the principal directions of the mean SGS stress tensor and alter the associated momentum transfer. Although not shown, this qualitative behavior persists throughout the FPG region. Since $\overline{\tau_{11}^{\rm sgs}}$, $\overline{\tau_{22}^{\rm sgs}}$, and $\overline{\tau_{12}^{\rm sgs}}$ are the three main components of the mean SGS stress tensor and others are negligible, only these are presented in the subsequent figures for clarity.

Figures 21 and 22 show the wall-normal distributions of the three main components of the mean SGS stress tensor at x/L = -0.1 for different mesh resolutions. In all cases, refining the mesh reduces the magnitude of the dominant SGS stress components and narrows the wall-normal region over which the SGS shear stress is significant.

For the SM, the dominant component of the mean SGS stress tensor is always the shear stress $\overline{\tau_{12}^{sgs}}$, regardless of mesh resolution. However, when the fine mesh is used, the normal stress components $\overline{\tau_{11}^{sgs}}$ and $\overline{\tau_{22}^{sgs}}$ become non-negligible in the near-wall region. This behavior indicates that the anisotropic dynamics of near-wall turbulence begin to be resolved, and the principal directions of both the mean SGS stress tensor and the mean strain-rate tensor shift relative to the coarser-mesh cases. Notably, the signs of these normal stress components are consistent with the MSM simulations, suggesting that the principal direction of the mean SGS stress in the fine-mesh SM case begins to align with that of the MSM.

For the MSM, by contrast, the near-wall dominance of $\overline{\tau_{12}^{\text{sgs}}}$, $\overline{\tau_{11}^{\text{sgs}}}$, and $\overline{\tau_{22}^{\text{sgs}}}$ is present at all mesh resolutions, and the qualitative behavior of these components remains unchanged with mesh refinement.

As mentioned earlier, the SGS stress provided by the MSM can be expressed as equation (2.4), consisting of an isotropic component $\tau_{ij}^{\rm iso}$ and an anisotropic component $\tau_{ij}^{\rm ani}$. Figure 23 shows the contributions of these two terms to the mean SGS stress at x/L = -0.1 for the medium-mesh MSM simulation. Again, only the three main components are plotted, since the remaining components are much smaller in magnitude.

The mean isotropic stress behaves almost identically to that in the SM case (see figure 20), indicating that adding the anisotropic term does not significantly modify the isotropic part of the model. A similar trend is also observed in the eddy-viscosity distributions within the FPG region (shown in figure 3). Moreover, since the SGS dissipation in the MSM arises exclusively from the isotropic stress term, this similarity implies that the SGS dissipation of kinetic energy is comparable between the SM and MSM at this location.

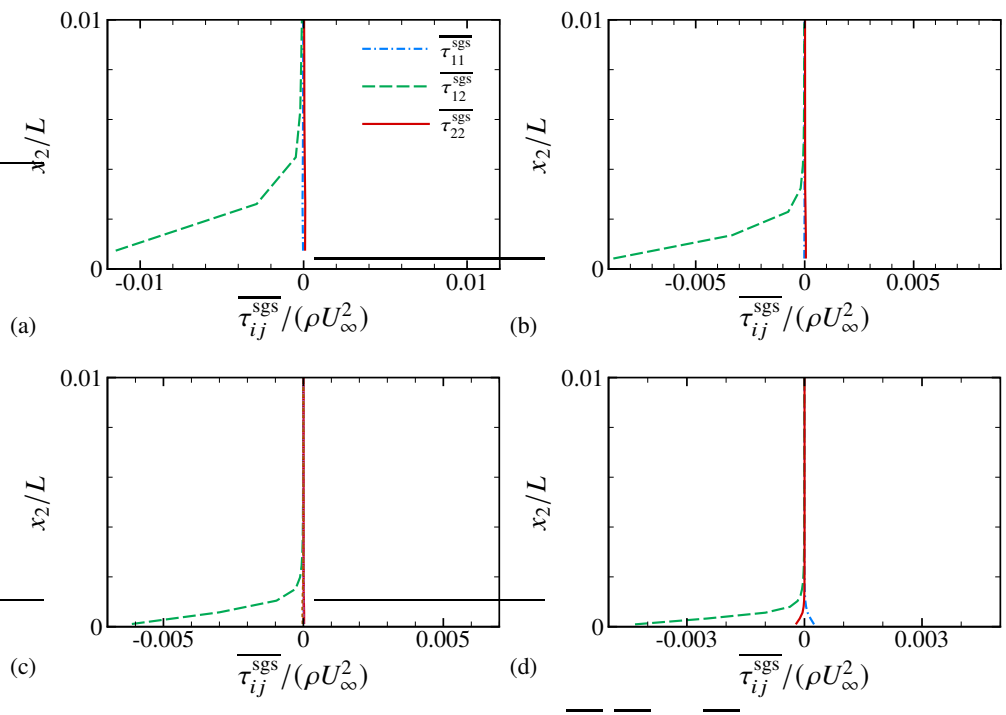


Figure 21: Mean SGS stress tensor components $(\overline{\tau_{11}^{\text{sgs}}}, \overline{\tau_{12}^{\text{sgs}}}, \text{ and } \overline{\tau_{22}^{\text{sgs}}})$ at x/L = -0.1 for simulations with the SM using the coarsest mesh (a), coarse mesh (b), medium mesh (c), and fine mesh (d).

In contrast, the mean anisotropic stress exhibits a distinctly different behavior, where the shear stress component are negligible while the normal stress components dominate. Comparing these results with the total mean SGS stress in figure 20 reveals that the normal stress in the MSM originate almost entirely from the anisotropic term. This confirms that the anisotropic SGS stress term is the primary source of the difference in the principal directions of the mean SGS stress tensor between the SM and MSM simulations.

The above comparison shows that the differences in the mean SGS stress between the SM and MSM arise from the normal stress components, $\overline{\tau_{11}^{sgs}}$ and $\overline{\tau_{22}^{sgs}}$, which originate from the additional anisotropic SGS stress term in the MSM. However, as shown in the mean streamwise momentum budget analysis in §4.1 and §4.4, these mean normal stresses have limited contributions to the mean streamwise momentum. In contrast, the mean shear stress component $\overline{\tau_{12}^{sgs}}$, which is the component most relevant to momentum transport and the onset of separation on relatively coarse meshes, is predicted similarly by both SGS models within the critical FPG region. This explains why the coarsest- and coarse-mesh simulations exhibit similar separation behavior for the SM and MSM.

5.2. SGS stress fluctuations

To obtain a more complete understanding of the SGS stress properties, it is also necessary to examine the SGS stress fluctuations, as these fluctuations can significantly influence the Reynolds stress distributions (see §4.3). Figure 24 shows the wall-normal distributions of the six independent components of the root-mean-square (r.m.s.) values of SGS stress fluctuations at x/L = -0.1 for the medium-mesh simulations. As with the mean SGS

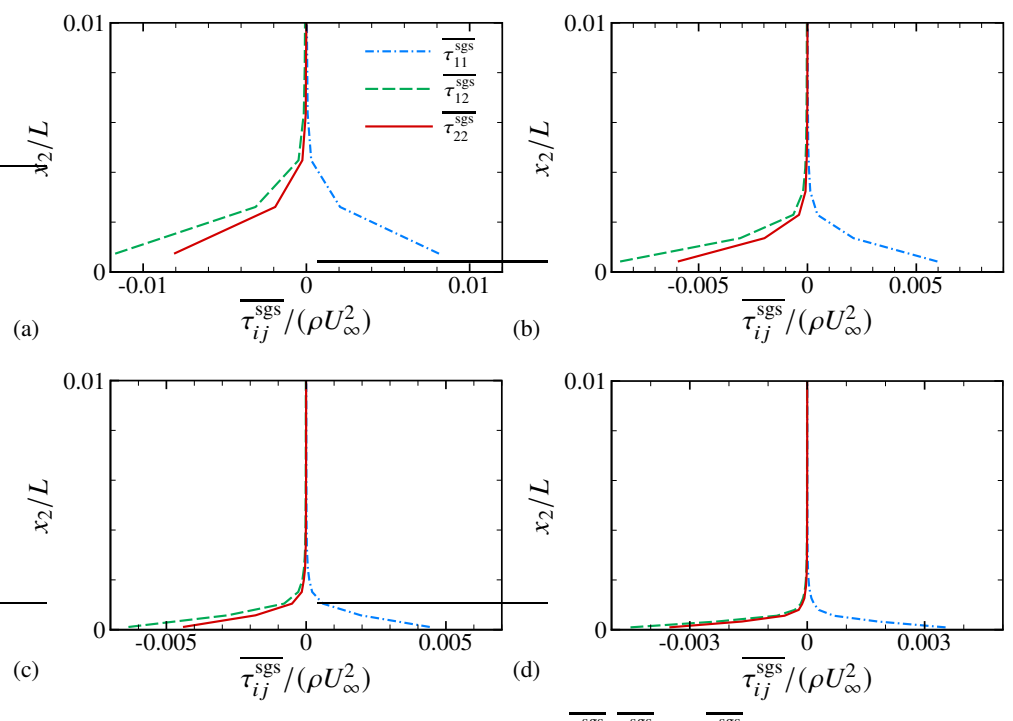


Figure 22: Mean SGS stress tensor components $(\overline{\tau_{11}^{sgs}}, \overline{\tau_{12}^{sgs}}, \text{ and } \overline{\tau_{22}^{sgs}})$ at x/L = -0.1 for simulations with the MSM using the coarsest mesh (a), coarse mesh (b), medium mesh (c), and fine mesh (d).

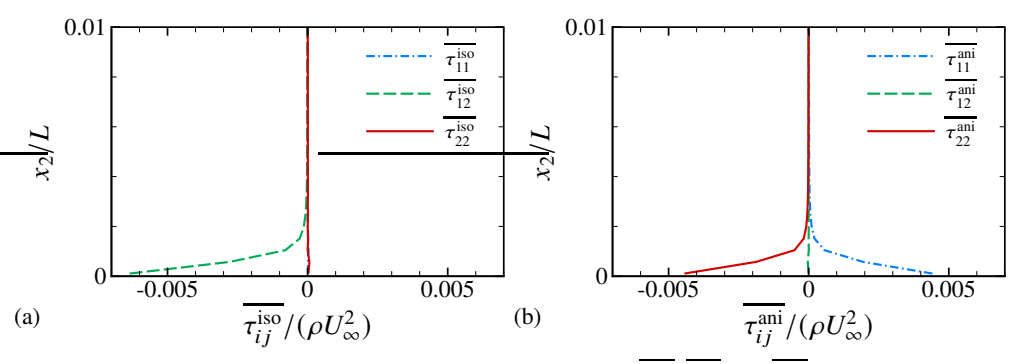


Figure 23: Mean isotropic SGS stress tensor components $(\overline{\tau_{11}^{\text{iso}}}, \overline{\tau_{12}^{\text{iso}}}, \text{ and } \overline{\tau_{22}^{\text{iso}}})$ (a) and mean anisotropic SGS stress tensor components $(\overline{\tau_{11}^{\text{ani}}}, \overline{\tau_{12}^{\text{ani}}}, \text{ and } \overline{\tau_{22}^{\text{ani}}})$ (b) at x/L = -0.1 for medium-mesh simulations with the MSM.

stresses, the SGS stress fluctuations are largest close to the wall, with τ_{12}^{sgs} exhibiting the strongest fluctuations in both simulations.

In the MSM simulation, however, the normal stress components τ_{11}^{sgs} and τ_{22}^{sgs} also display substantial fluctuations, unlike in the SM. Because fluctuations of the normal stresses contribute directly to both SGS dissipation and SGS diffusion in the Reynolds stress transport equation, these enhanced fluctuations help explain the distinct SGS dissipation and diffusion behavior observed for the MSM in §4.3. Examination at other streamwise locations shows

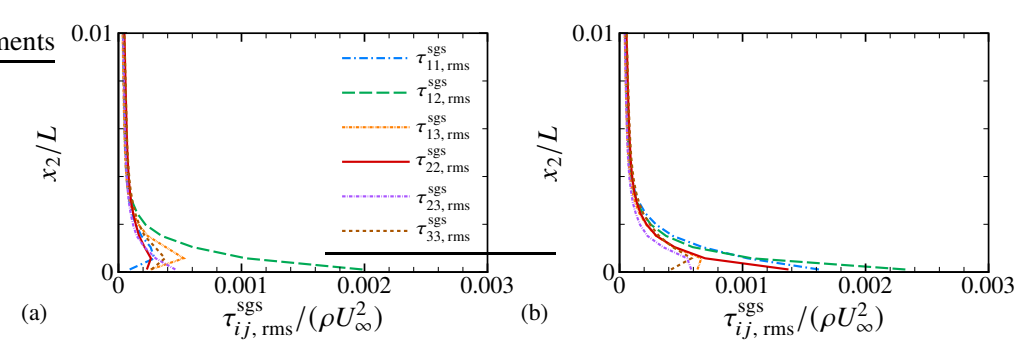


Figure 24: SGS stress tensor r.m.s. components $\tau_{ij,\,\mathrm{rms}}^{\mathrm{sgs}}$ at x/L = -0.1 for medium-mesh simulations with the SM (a) and MSM (b).

that this qualitative behavior of SGS stress fluctuations remains largely consistent throughout the FPG region.

Figures 25 and 26 show the r.m.s. values of the SGS stress fluctuations at x/L = -0.1 for simulations using different mesh resolutions with the SM and MSM, respectively. Here, only the results corresponding to the three main components are exhibited. Within each SGS model, the qualitative behavior of the fluctuations remains similar as the mesh is refined. In contrast to the mean SGS stresses, which decrease rapidly with mesh refinement, the magnitudes of SGS stress fluctuations only mildly decrease with refinement. This difference in scaling implies that the relative importance of SGS stress fluctuations increases as the grid is refined. Furthermore, at this streamwise location, the MSM consistently produces larger fluctuations in all these SGS stress components than the SM for a given mesh resolution.

For the MSM simulations, we further examined the SGS stress fluctuations at x/L = -0.1 by separating the isotropic and anisotropic contributions, shown in figure 27. Similar to the mean SGS stress results, the fluctuations associated with the isotropic term behave similarly to those in the SM (see figure 25), again indicating that the addition of the anisotropic term does not substantially alter the isotropic component of the model. In contrast, the fluctuations of anisotropic stress term are dominated by the normal stress components $\tau_{11}^{\rm ani}$ and $\tau_{22}^{\rm ani}$, consistent with the behavior of the mean anisotropic stress. Comparison with the total SGS stress fluctuations shown in figure 26 reveals that the large fluctuations in these normal components primarily originate from the anisotropic term.

These observations confirm that the differences in SGS dissipation and diffusion of Reynolds stresses discussed in §4.3 stem mainly from the additional anisotropic stress term in the MSM, not from modifications to the isotropic stress term. This also suggests that optimizing the formulation of the anisotropic stress term in anisotropic SGS models may provide an effective means of controlling SGS stress fluctuations and, in turn, improving the prediction of Reynolds stress distributions and the mean velocity field.

5.3. A priori analysis of filtered DNS

Previously, based on a series of WMLES, we conducted a comprehensive *a posteriori* analysis of the mean SGS stress and the fluctuations of SGS stress within the critical FPG region on the windward side of the bump. To further validate those conclusions and to gain additional insight into the characteristics of SGS stress in wall-bounded turbulence under FPG, we perform an *a priori* analysis using Gaussian-filtered DNS of turbulent Couette-Poiseuille flow. The DNS is conducted at a Reynolds number of $Re_H = U_c H/v = 2,500$, where H is

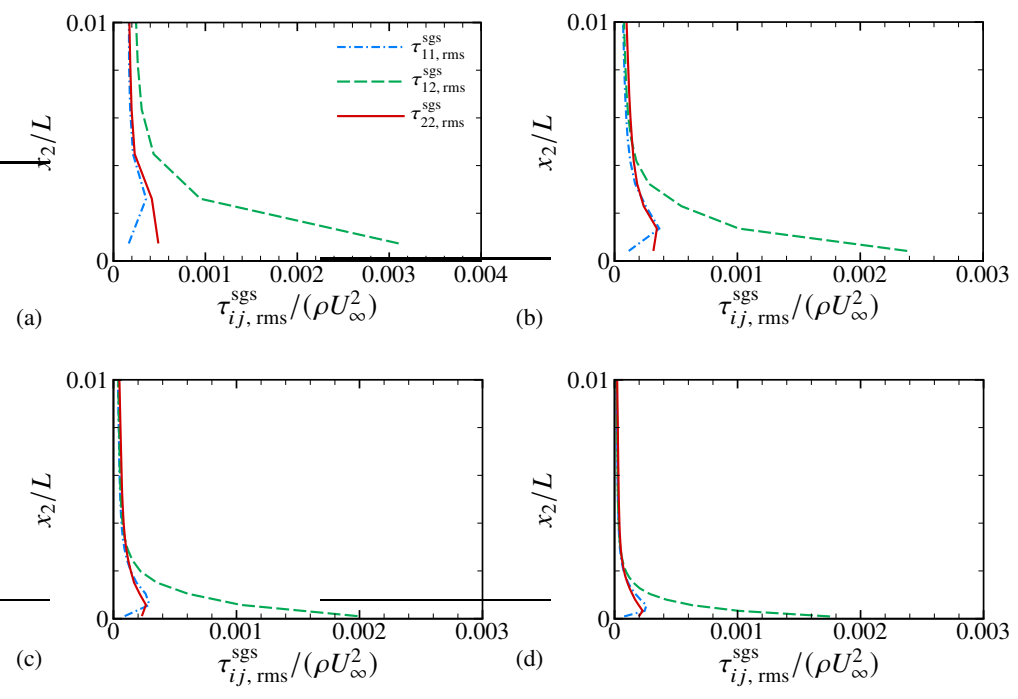


Figure 25: SGS stress tensor r.m.s. components ($\tau_{11,\,\mathrm{rms}}^{\mathrm{sgs}}$, $\tau_{12,\,\mathrm{rms}}^{\mathrm{sgs}}$, and $\tau_{22,\,\mathrm{rms}}^{\mathrm{sgs}}$) at x/L = -0.1 for simulations with the SM using the coarsest mesh (a), coarse mesh (b), medium mesh (c), and fine mesh (d).

the half-channel height and U_c is the wall motion speed. Additional details of the DNS and the filtering operation are provided in Sections C and D.

The *a priori* analysis focuses on the lower half of the channel, where the flow near the bottom wall experiences an FPG and behaves qualitatively similarly to a TBL with FPG. Gaussian filtering of the velocity field is applied only in the streamwise (x) and spanwise (z) directions, since the DNS grid is non-uniform in the wall-normal (y) direction. To examine a range of moderate to coarse filter widths, the standard deviations of the Gaussian kernel are set to $\sigma_x/\Delta_x = \sigma_z/\Delta_z = 1$, 2 and 4, where Δ_x and Δ_z are the uniform DNS grid spacings in x and z. Based on the filtered velocity field, the SGS stress can be calculated as $\tau_{ij}^{\rm sgs} = \widehat{u_i u_j} - \widehat{u_i} \widehat{u_j}$, where $\widehat{(\cdot)}$ denotes Gaussian filtering. For the present analysis, we only consider the deviatoric, trace-free part of the SGS stress tensor.

Figure 28(a) shows the wall-normal distributions of the mean SGS stress components obtained from the filtered DNS data using a Gaussian kernel with $\sigma_x/\Delta_x = \sigma_z/\Delta_z = 2$. The magnitudes of the mean SGS stresses are largest near the wall, with peak values occurring at $y/H \approx 0.06$ (approximately 20 wall units). A key observation is that the normal stress components, $\tau_{11}^{\rm sgs}$ and $\tau_{22}^{\rm sgs}$, are significantly larger than the other components. This indicates strong SGS anisotropy near the wall, with the streamwise and wall-normal directions dominating the interscale energy transfer. By contrast, although the mean shear is large in this region, the small-scale cross-correlation between streamwise and wall-normal velocity fluctuations is weaker than the variance of each component, causing the mean shear stress $\tau_{12}^{\rm sgs}$ to remain comparatively small.

When compared with the mean SGS stress in the TBL within the FPG region of the present WMLES, the filtered DNS results exhibit behavior more consistent with the MSM

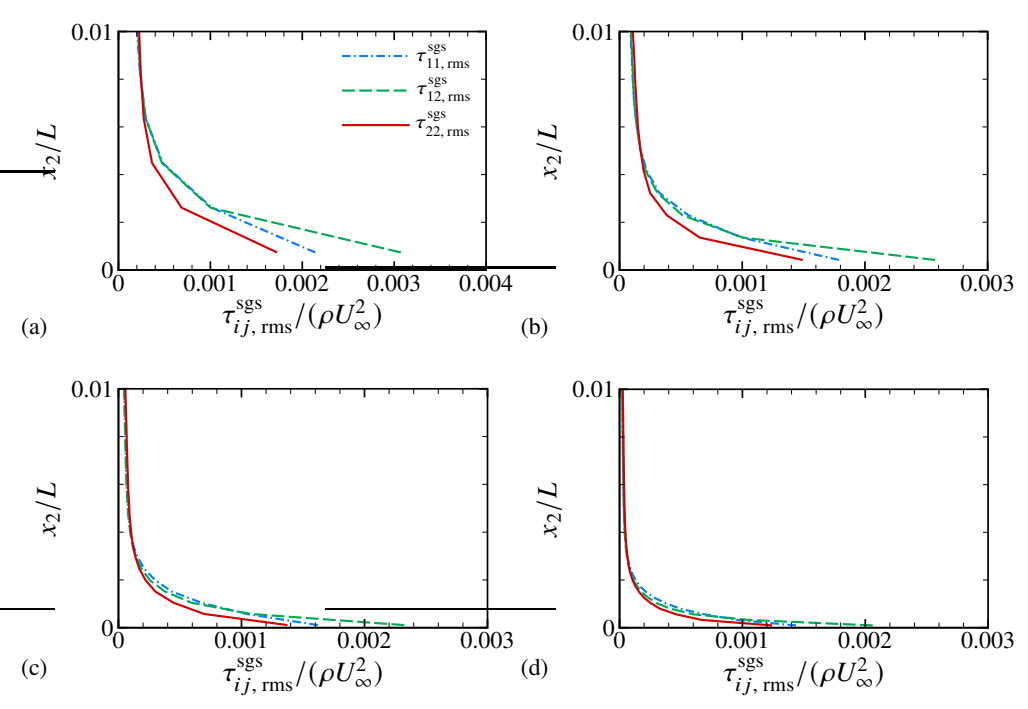


Figure 26: SGS stress tensor r.m.s. components ($\tau_{11, \, \text{rms}}^{\text{sgs}}$, $\tau_{12, \, \text{rms}}^{\text{sgs}}$, and $\tau_{22, \, \text{rms}}^{\text{sgs}}$) at x/L = -0.1 for simulations with the MSM using the coarsest mesh (a), coarse mesh (b), medium mesh (c), and fine mesh (d).

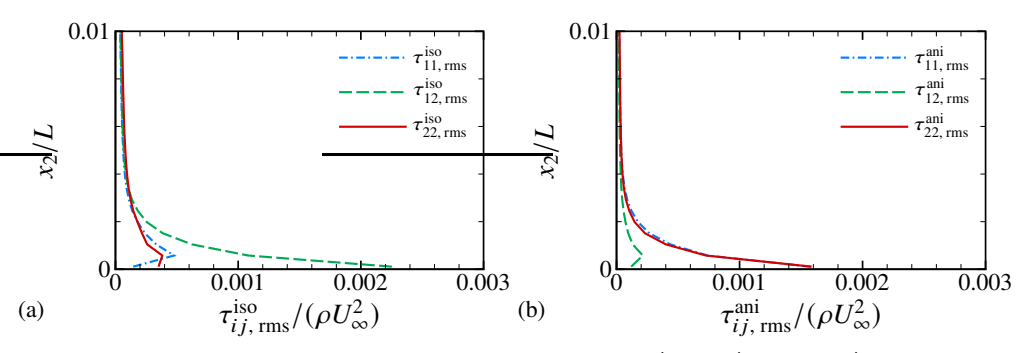


Figure 27: Isotropic SGS stress tensor r.m.s. components ($\tau_{11,~\rm rms}^{\rm iso}$, $\tau_{12,~\rm rms}^{\rm iso}$, and $\tau_{22,~\rm rms}^{\rm iso}$) (a) and anisotropic SGS stress tensor r.m.s. components ($\tau_{11,~\rm rms}^{\rm ani}$, $\tau_{12,~\rm rms}^{\rm ani}$, and $\tau_{22,~\rm rms}^{\rm ani}$) (b) at x/L=-0.1 for medium-mesh simulations with the MSM.

predictions. In both cases, the anisotropic stress introduces crucial normal stress components in the near-wall region, and the signs of the dominant $\tau_{11}^{\rm sgs}$ and $\tau_{22}^{\rm sgs}$ components agree between the two flows. However, due to the coarse resolution along the wall-normal direction in the WMLES, the peaks of the mean SGS stress components are not fully captured.

It is also worth noting that the qualitative behavior of the mean SGS stresses remains similar across different standard deviations of the Gaussian filter, or equivalently, different effective filter widths. For brevity, results for other filter widths (e.g., $\sigma_x/\Delta_x = \sigma_z/\Delta_z = 1$ or 4) are not shown. Examination of these cases indicates that increasing the filter standard

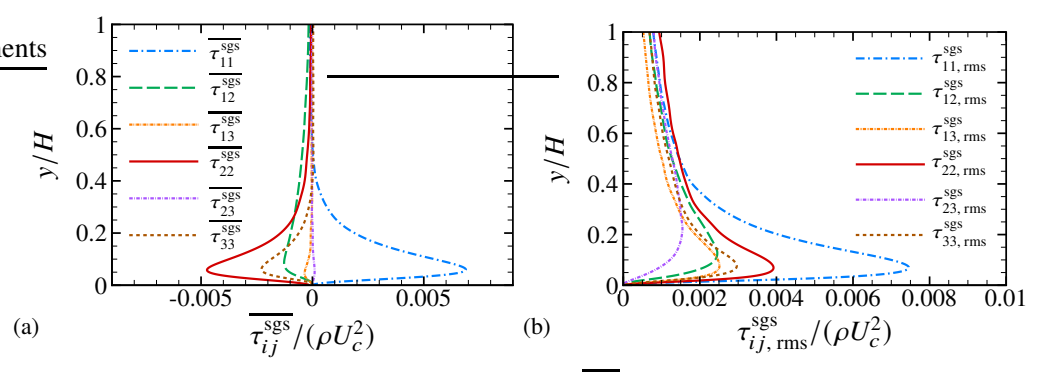


Figure 28: Mean SGS stress tensor components $\overline{\tau}_{ij}^{\text{sgs}}$ (a) and SGS stress tensor r.m.s. components $\tau_{ij,\,\text{rms}}^{\text{sgs}}$ (b) obtained from the Gaussian filtering of velocity field from the DNS of turbulent Couette-Poiseuille flow with the standard deviations of the Gaussian kernel $\sigma_x/\Delta_x = \sigma_z/\Delta_z = 2$.

deviation leads to larger mean SGS stress magnitudes, consistent with the fact that wider filters remove more turbulent scales and therefore attribute a greater portion of the momentum transfer to the unresolved motions.

Figure 28(b) shows the wall-normal distributions of the r.m.s. values of SGS stress fluctuations from filtered DNS. As expected, the fluctuation intensities are largest near the bottom wall, with peak values occurring at approximately the same wall-normal location as the mean SGS stresses in figure 28(a). While the mean SGS stresses represent the average interscale momentum transfer, the r.m.s. values reflect its temporal and spatial variability and are therefore more sensitive to localized turbulent events. The strong peaks near the wall indicate that the energy transfer between resolved and subgrid scales is highly intermittent in this region, driven by the bursting and ejection–sweep cycles characteristic of near-wall turbulence. The particularly large fluctuations in $\tau_{11}^{\rm sgs}$ and $\tau_{22}^{\rm sgs}$ suggest substantial temporal variability in the normal stress components, likely associated with rapid distortion of streaks and vortical structures.

The strong normal SGS stress fluctuations are also better captured by the MSM in the WMLES, whereas they are nearly absent in the SM results within the FPG region. This reinforces the role of the anisotropic stress term in reproducing the correct near-wall SGS dynamics. Finally, although results for other filter widths $(\sigma_x/\Delta_x = \sigma_z/\Delta_z = 1 \text{ and 4})$ are not shown, their qualitative behavior is similar: the fluctuation intensities increase with filter width, consistent with the enhanced contribution from unresolved scales.

From the filtered DNS analysis and its comparison with the WMLES results, it is evident that in wall-bounded turbulence under FPG the SGS dynamics are strongly anisotropic near the wall, with the normal SGS stress components playing a major role. Classical eddy-viscosity models are unable to represent these effects adequately. In contrast, the anisotropic SGS model reproduces the near-wall anisotropy much more realistically, consistent with the characteristics observed in the filtered DNS. These findings suggest that improving or optimizing the anisotropic stress term in SGS models offers a promising pathway for enhancing model performance in simulations of complex turbulent flows.

6. Conclusions

This study performed a comprehensive *a posteriori* analysis of the effect of anisotropic SGS stress on WMLES of separated turbulent flow over a spanwise-uniform Gaussian bump. An

idealized wall boundary condition prescribing the local mean wall-shear stress from DNS data (Uzun & Malik 2022) was used to isolate the impact of the SGS model. Two models were compared: the classical Smagorinsky model (SM) and a modified Smagorinsky model (MSM) that includes an additional anisotropic stress term.

The main findings are summarized as follows. First, the predicted flow separation on the leeward side of the bump depends strongly on the SGS model. The isotropic SM exhibits non-monotonic convergence of the mean separation bubble length with mesh refinement, whereas the anisotropic MSM provides consistent predictions across resolutions. Second, the influence of anisotropic SGS stress is found to be most critical upstream of the bump peak, within the region of strong favorable pressure gradient (FPG). Changes to the SGS model in this region substantially alter the downstream separation, revealing a pronounced history effect in determining separation onset. Third, inclusion of anisotropic SGS stress improves the prediction of Reynolds shear and normal stress distributions in the FPG region. These modifications propagate downstream and influence the onset and size of the separation bubble. Analysis of the Reynolds stress budget shows that anisotropic SGS stress fluctuations enable both dissipation and backscatter, facilitating the bidirectional energy transfer that isotropic models fail to represent. The dependence of flow-separation prediction on mesh resolution is also clarified. On coarse meshes, the mean SGS shear stress dominates the streamwise momentum balance upstream of the separation point, and both models behave similarly. As the resolution increases, Reynolds stresses become more influential, and the anisotropic MSM better captures their distribution and yields more consistent flow predictions. At fine resolution, model differences diminish as more turbulent scales are resolved. The key physical distinction between the SM and MSM arises from the normal SGS stress components, τ_{11}^{sgs} and τ_{22}^{sgs} , which in the MSM significantly contribute to SGS dissipation and diffusion of Reynolds stresses, particularly under FPG. An a priori analysis based on filtered DNS of Couette-Poiseuille flow further confirms that near-wall turbulence under FPG is highly anisotropic and dominated by these normal stress components, which are not captured by isotropic eddy-viscosity models.

Taken together, these findings explain why isotropic and anisotropic SGS models yield qualitatively different predictions of separation behavior and why the anisotropic model achieves more consistent convergence across mesh resolutions. The results emphasize that accurate WMLES predictions require proper representation of both mean and fluctuating SGS stresses, especially their anisotropy in the near-wall region.

Beyond elucidating the role of anisotropic SGS stress, this study highlights directions for improving WMLES of complex wall-bounded turbulence. Since the unresolved motions in WMLES carry substantial energy and momentum fluxes, the SGS model must account for anisotropic stress dynamics near the wall and under pressure gradients. Developing more advanced anisotropic SGS models, potentially through optimized extensions of eddy-viscosity formulations (Marstorp *et al.* 2009; Silvis & Verstappen 2019; Agrawal *et al.* 2022; Uzun & Malik 2025), is therefore a promising path forward. Although this work employed an idealized wall model to isolate SGS effects, realistic wall modeling and its coupling with the SGS model remain critical challenges. Unified SGS/wall modeling frameworks (Ling *et al.* 2022; Arranz *et al.* 2023, 2024; Zhou *et al.* 2025) represent a promising direction to enhance the robustness and predictive accuracy of WMLES for complex turbulent flows.

Acknowledgments

This work was supported by National Science Foundation (NSF) grant No. 2152705. Computer time was provided by the Discover project at Pittsburgh Supercomputing Center through allocation PHY240020 from the Advanced Cyberinfrastructure Coordination Ecosystem:

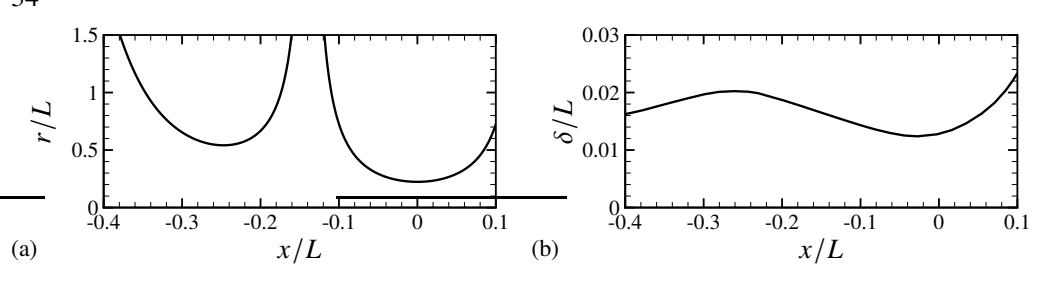


Figure 29: Curvature radius (a) of the Gaussian bump surface and local boundary layer thickness (b) for the medium-mesh simulation with the SM in $x/L \in [-0.4, 0.1]$.

Services & Support (ACCESS) program, which is supported by NSF grants No. 2138259, No. 2138286, No. 2138307, No. 2137603, and No. 2138296. The authors sincerely thank Dr. Ali Uzun and Dr. Mujeeb Malik for generously sharing their DNS data. We also extend our special gratitude to Dr. Meng Wang for his invaluable assistance.

Declaration of Interests

The authors report no conflict of interest.

Appendix A. Investigation of the curvature effect on the region upstream of separation

Figure 29 shows the local curvature radius (r) of the present Gaussian bump surface and the local boundary layer thickness (δ) from the medium-mesh simulation with the SM in the region $x/L \in [-0.4, 0.1]$. The curvature radius reaches its minimum at the bump peak (x/L = 0), where the curvature is largest, while the curvature radius is substantially larger at all other locations. Even at the bump peak, the minimum curvature radius remains much larger than the local boundary layer thickness, with the ratio of curvature radius to boundary layer thickness exceeding 10. These observations indicate that curvature effects in this region are negligible, consistent with findings of previous studies (Prakash *et al.* 2024; Spalart *et al.* 2024).

Appendix B. Simulations using the mixed model

An additional anisotropic SGS model evaluated in the present study is the mixed model (MM) (Bardina 1983; Sarghini *et al.* 1999). It combines the SM (Smagorinsky 1963) with a scale-similarity term computed using explicit filtering (Meneveau & Katz 2000), which is given by

$$\tau_{ij}^{\text{ani}} = \widehat{u_i u_j} - \hat{u}_i \,\hat{u}_j \,, \tag{B 1}$$

where $\widehat{(\cdot)}$ denotes an explicit filtering operation, chosen here as Gaussian filtering. With the use of Gaussian filtering, the anisotropic term can be approximated (Clark *et al.* 1979) by

$$\tau_{ij}^{\rm ani} = \widehat{u_i u_j} - \hat{u}_i \, \hat{u}_j \approx \frac{\Delta^2}{12} \frac{\partial u_i}{\partial x_k} \frac{\partial u_j}{\partial x_k} = \frac{\Delta^2}{12} \left[S_{ik} S_{kj} - R_{ik} R_{kj} - \left(S_{ik} R_{kj} - R_{ik} S_{kj} \right) \right] \; . \eqno(B 2)$$

In addition to introducing anisotropic SGS stress, this term can produce kinetic energy dissipation. In particular, it can also produce negative dissipation, which allows for local backscatter of kinetic energy. The isotropic SGS stress term in the MM is given by the SM with a coefficient of $C_s = 0.127$ (Bhushan & Warsi 2005; Bhushan *et al.* 2006), chosen to

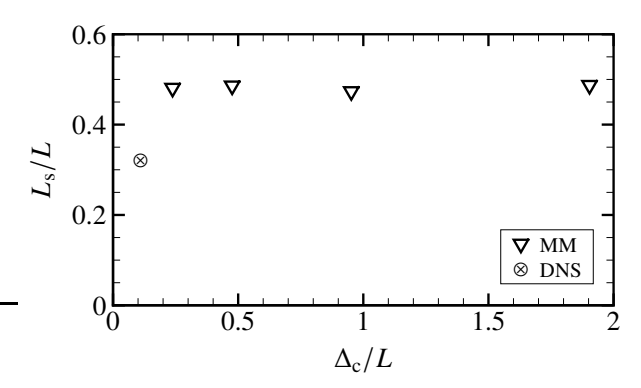


Figure 30: Mean separation bubble length on the leeward side of the bump from the simulations using the MM for different mesh resolutions and the reference DNS (Uzun & Malik 2022). Symbols represent data point for each case.

ensure that the total kinetic energy dissipation for homogeneous isotropic turbulence from both the isotropic and anisotropic stress terms matches that from the SM and MSM used in the present study. The MM simulations are carried out using the same computational meshes and boundary conditions described in §2.

Figure 30 shows the mean separation bubble length on the leeward side of the bump as a function of characteristic mesh resolution. The MM simulations consistently overpredict the separation bubble length, but the predictions that remain nearly insensitive to mesh refinement. This trend mirrors the behavior observed for the MSM simulations (see figure 7), further underscoring the robustness of anisotropic SGS models for WMLES.

Additional analyses of the mean streamwise momentum, mean pressure, and Reynolds stress transport equations using data from multiple mesh resolutions show that the MM exhibits behavior qualitatively similar to the MSM, particularly in its representation of anisotropic stress effects. Thus, the conclusions drawn in the main text remain applicable to the MM simulations.

Appendix C. DNS of plane Couette-Poiseuille flow

A DNS of turbulent plane Couette–Poiseuille flow is conducted at $Re_H = 2,500$, where H denotes the half-channel height. In the simulation, the incompressible Navier–Stokes equations are solved using a staggered finite-difference scheme that is second-order accurate in space and advanced in time with an explicit third-order Runge–Kutta method. The flow solver has been validated in previous studies of turbulent channel flows (Bae *et al.* 2018, 2019). In the computational domain, periodic boundary conditions are imposed in the streamwise (x) and spanwise (z) directions. The top and bottom walls move parallel to each other in opposite directions along the x axis. A Dirichlet boundary condition with constant velocity $u_x = U_c = 1$ is applied at the top wall (y/H = 2), while a constant velocity $u_x = -U_c = -1$ is imposed at the bottom wall (y/H = 0). A constant streamwise pressure gradient, corresponding to $H/(\rho U_c^2)\frac{dp}{dx} = -0.003$, is applied to drive the flow, indicating that the mean pressure decreases in the positive x direction. The computational domain extends over $L_x/H = 6\pi$, $L_y/H = 2$, and $L_z/H = 3\pi$ in the streamwise, wall-normal, and spanwise directions, respectively. Uniform grids with 512 points are used in both the streamwise and spanwise directions. In the wall-normal direction, 256 non-uniformly spaced points are distributed according to a hyperbolic tangent stretching, yielding $\min(\Delta y)/H = 3.5 \times 10^{-4}$ and $\max(\Delta y)/H = 2.2 \times 10^{-2}$. The simulation is first advanced

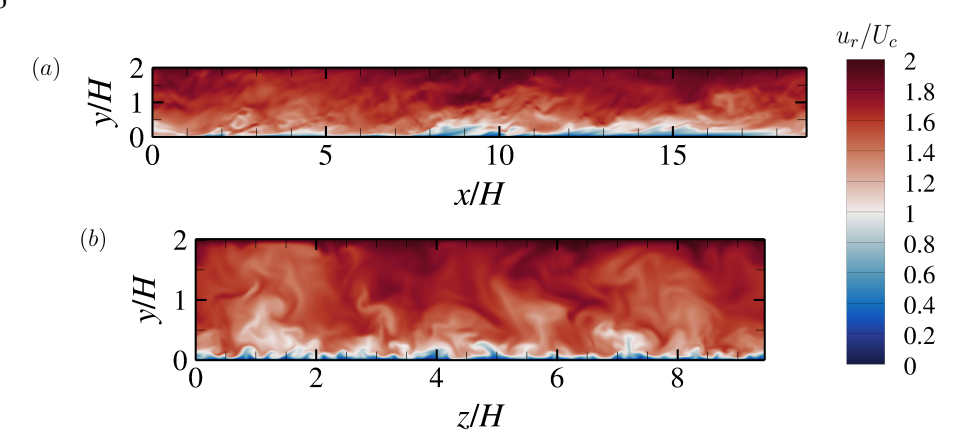


Figure 31: Isocontours of the instantaneous streamwise velocity relative to the bottom wall u_r/U_c in (a) an x-y plane and (b) a z-y plane from the DNS of turbulent Couette–Poiseuille flow.

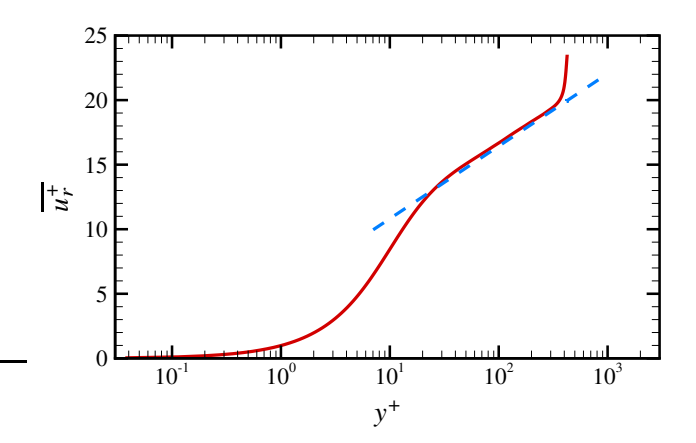


Figure 32: Mean streamwise velocity relative to the bottom wall from the DNS of turbulent Couette-Poiseuille flow. The dashed line represents the classical log law of the wall $\overline{u_r^+} = (1/0.41) \ln(y^+) + 5.2$.

for 100 flow-through times ($6\pi H/U_c$) to eliminate initial transients. After the flow reaches a statistically stationary state, 1,500 temporal snapshots are collected for the present analysis. Moreover, the statistical quantities in the present study are obtained by performing temporal and spatial averaging along the homogeneous streamwise and spanwise directions of the corresponding instantaneous fields.

Figure 31 shows the instantaneous streamwise velocity relative to the bottom wall, $u_r = u_x + U_c$, from the DNS. Due to the motion of the parallel walls and the imposed mean pressure gradient, the wall-bounded turbulence in the upper half of the channel experiences an APG and behaves similarly to an APG TBL containing many large-scale flow structures. In contrast, the turbulence near the bottom wall is subjected to an FPG and qualitatively similar to an FPG TBL. Figure 32 presents the profile of inner-scaled mean streamwise velocity relative to the bottom wall, defined as $\overline{u_r} = \overline{(u_x + U_c)/u_{\tau,b}}$. Here, the superscript "+" denotes inner-scaled quantity by wall unit and $u_{\tau,b}$ is the bottom-wall friction velocity.

Appendix D. Filtering of the DNS velocity field

To obtain the filtered velocity field from the DNS of the turbulent Couette–Poiseuille flow, a Gaussian filter is applied to the instantaneous velocity field $\mathbf{u} = (u_x, u_y, u_z)$. Since the DNS grid is non-uniform in the wall-normal (y) direction, the filtering operation is performed only in the streamwise (x) and spanwise (z) directions to avoid commutation errors. The filtered velocity field $\widehat{\mathbf{u}} = (\widehat{u}_x, \widehat{u}_y, \widehat{u}_z)$ is obtained through a two-dimensional convolution in the x and z directions,

$$\widehat{u}_i(x, y, z) = \iint G(x - r_x, z - r_z) \, u_i(r_x, y, r_z) \, dr_x \, dr_z \,, \tag{D 1}$$

where the Gaussian kernel is defined as

$$G(r_x, r_z) = \frac{1}{2\pi \sigma_x \sigma_z} \exp\left[-\frac{1}{2} \left(\frac{r_x^2}{\sigma_x^2} + \frac{r_z^2}{\sigma_z^2}\right)\right]. \tag{D2}$$

Here, r_x and r_z denote spatial separations in the streamwise and spanwise directions, and σ_x and σ_z are the corresponding standard deviations of the Gaussian kernel. Since the DNS grid is uniform in both directions, the filtering is implemented as a discrete convolution using symmetric one-dimensional Gaussian kernels applied successively in x and z.

The effective filter width $\Delta_{f,i}$ in each direction $i \in \{x, z\}$ is defined by matching the second moment of the Gaussian filter with that of a top-hat filter, giving

$$\Delta_{f,i} = 2\sqrt{3}\,\sigma_i \,. \tag{D3}$$

In this study, the standard deviations are set as multiples of the uniform DNS grid spacings such that $\sigma_x/\Delta_x = \sigma_z/\Delta_z = 1$, 2, and 4, corresponding to moderate to coarse filter widths that remove small-scale motions while retaining large-scale flow structures. The resulting effective filter widths $\Delta_{f,x}$ and $\Delta_{f,z}$ are approximately 3.464, 6.928, and 13.856 times the grid spacings Δx and Δz , respectively.

Figure 33 shows the filtered instantaneous streamwise velocity relative to the bottom wall \widehat{u}_r/U_c in an x-y plane for these three filter widths, along with the DNS field. As the standard deviations increase, progressively finer structures are removed, demonstrating how the Gaussian filter systematically isolates the larger-scale motions.

REFERENCES

ABE, K. 2013 An improved anisotropy-resolving subgrid-scale model with the aid of a scale-similarity modeling concept. *Int. J. Heat Fluid Flow* **39**, 42–52.

ABE, K. 2014 An investigation of SGS stress anisotropy modeling in complex turbulent flow fields. *Flow Turbul. Combust.* **92** (1), 503–525.

ABE, K. 2019 Notable effect of the subgrid-scale stress anisotropy on mean-velocity prediction through budget of the grid-scale Reynolds-shear stress. *Phys. Fluids* **31** (10), 105103.

AGRAWAL, R., Bose, S. T. & Moin, P. 2024 Reynolds-number-dependence of length scales governing turbulent-flow separation in wall-modeled large eddy simulation. *AIAA J.* **62** (10), 3686–3699.

AGRAWAL, R., WHITMORE, M. P., GRIFFIN, K. P., Bose, S. T. & MOIN, P. 2022 Non-Boussinesq subgrid-scale model with dynamic tensorial coefficients. *Phys. Rev. Fluids* 7 (7), 074602.

Arranz, G., Ling, Y., Costa, S., Goc, K. & Lozano-Durán, A. 2024 Building-block-flow computational model for large-eddy simulation of external aerodynamic applications. *Commun. Eng.* 3 (1), 127.

Arranz, G., Ling, Y. & Lozano-Duran, A. 2023 Wall-modeled LES based on building-block flows: Application to the Gaussian bump. In *AIAA Aviation 2023 Forum*, p. 3984.

BAE, H. J., LOZANO-DURÁN, A., BOSE, S. T. & MOIN, P. 2018 Turbulence intensities in large-eddy simulation of wall-bounded flows. *Phys. Rev. Fluids* 3 (1), 014610.

BAE, H. J., LOZANO-DURÁN, A., BOSE, S. T. & MOIN, P. 2019 Dynamic slip wall model for large-eddy simulation. *J. Fluid Mech.* **859**, 400–432.

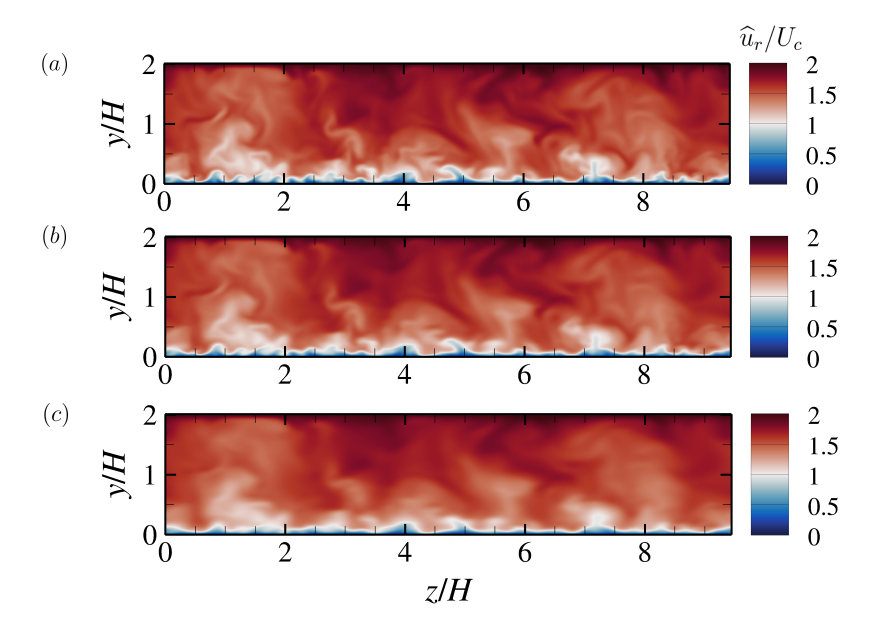


Figure 33: Isocontours of the filtered streamwise velocity \widehat{u}_r/U_c with $\sigma_x/\Delta x = \sigma_z/\Delta z = 1$ (a), 2 (b), and 4 (c).

Balin, R. & Jansen, K. E. 2021 Direct numerical simulation of a turbulent boundary layer over a bump with strong pressure gradients. *J. Fluid Mech.* **918**, A14.

Bardina, J. 1983 Improved turbulence models based on large eddy simulation of homogeneous, incompressible turbulent flows. Stanford University.

Bhushan, S. & Warsi, Z. U. A. 2005 Large eddy simulation of turbulent channel flow using an algebraic model. *Int. J. Numer. Methods Fluids* **49** (5), 489–519.

Bhushan, S., Warsi, Z. U. A. & Walters, D. K. 2006 Modeling of energy backscatter via an algebraic subgrid-stress model. *AIAA J.* **44** (4), 837–847.

Bose, S. T. & Moin, P. 2014 A dynamic slip boundary condition for wall-modeled large-eddy simulation. *Phys. Fluids* **26** (1), 015104.

Bose, S. T. & Park, G. I. 2018 Wall-modeled large-eddy simulation for complex turbulent flows. *Annu. Rev. Fluid Mech.* **50**, 535–561.

Choi, H., Cho, C., Kim, M. & Park, J. 2025 Perspective on machine-learning-based large-eddy simulation. *Phys. Rev. Fluids* **10** (11), 110701.

Choi, H. & Moin, P. 2012 Grid-point requirements for large eddy simulation: Chapman's estimates revisited. *Phys. Fluids* **24** (1), 011702.

CIMARELLI, A., LEONFORTE, A., DE ANGELIS, E., CRIVELLINI, A. & ANGELI, D. 2019 Resolved dynamics and subgrid stresses in separating and reattaching flows. *Phys. Fluids* **31** (9), 095101.

CLARK, R. A., FERZIGER, J. H. & REYNOLDS, W. C. 1979 Evaluation of subgrid-scale models using an accurately simulated turbulent flow. *J. Fluid Mech.* **91** (1), 1–16.

Domaradzki, J. A. & Saiki, E. M. 1997 A subgrid-scale model based on the estimation of unresolved scales of turbulence. *Phys. Fluids* **9** (7), 2148–2164.

Duraisamy, K. 2021 Perspectives on machine learning-augmented Reynolds-averaged and large eddy simulation models of turbulence. *Phys. Rev. Fluids* **6** (5), 050504.

GATSKI, T. B. & JONGEN, T. 2000 Nonlinear eddy viscosity and algebraic stress models for solving complex turbulent flows. *Prog. Aerosp. Sci.* **36** (8), 655–682.

GLUZMAN, I., GRAY, P. D., MEJIA, K., CORKE, T. C. & THOMAS, F. O. 2022 A simplified photogrammetry procedure in oil-film interferometry for accurate skin-friction measurement over arbitrary geometries. *Exp. Fluids* **63** (7), 118.

Goc, K. A., Lehmkuhl, O., Park, G. I., Bose, S. T. & Moin, P. 2021 Large eddy simulation of aircraft at affordable cost: a milestone in computational fluid dynamics. *Flow* 1, E14.

- Goc, K. A., Moin, P., Bose, S. T. & Clark, A. M. 2024 Wind tunnel and grid resolution effects in large-eddy simulations of the high-lift common research model. *J. Aircr.* **61** (1), 267–279.
- Gray, P. D., Gluzman, I., Thomas, F. O. & Corke, T. C. 2022a Experimental characterization of smooth body flow separation over wall-mounted Gaussian bump. In *AIAA Scitech 2022 Forum*, p. 1209.
- Gray, P. D., Gluzman, I., Thomas, F. O., Corke, T. C., Lakebrink, M. T. & Mejia, K. 2021 A new validation experiment for smooth-body separation. In *AIAA Aviation 2021 Forum*, p. 2810.
- Gray, P. D., Gluzman, I., Thomas, F. O., Corke, T. C., Lakebrink, M. T. & Mejia, K. 2022b Benchmark characterization of separated flow over smooth Gaussian bump. In *AIAA Aviation 2022 Forum*, p. 3342.
- HAERING, S. W., LEE, M. & Moser, R. D. 2019 Resolution-induced anisotropy in large-eddy simulations. *Phys. Rev. Fluids* **4** (11), 114605.
- HORIUTI, K. 1997 A new dynamic two-parameter mixed model for large-eddy simulation. *Phys. Fluids* **9** (11), 3443–3464.
- HORIUTI, K. 2003 Roles of non-aligned eigenvectors of strain-rate and subgrid-scale stress tensors in turbulence generation. *J. Fluid Mech.* **491**, 65–100.
- INAGAKI, K. & KOBAYASHI, H. 2020 Role of various scale-similarity models in stabilized mixed subgrid-scale model. *Phys. Fluids* **32** (7).
- INAGAKI, K. & KOBAYASHI, H. 2023 Analysis of anisotropic subgrid-scale stress for coarse large-eddy simulation. *Phys. Rev. Fluids* **8** (10), 104603.
- IYER, P. S. & MALIK, M. R. 2022 Wall-modeled LES of turbulent flow over a two dimensional Gaussian bump. In *Eleventh International Conference on Computational Fluid Dynamics*, p. 0204.
- IYER, P. S. & MALIK, M. R. 2024 Efficient dynamic mixed subgrid-scale model. *Phys. Rev. Fluids* **9** (9), L092601.
- IYER, P. S. & MALIK, M. R. 2025 Insights from targeted grid refinement for WMLES of turbulent smooth-body separation. *Flow Turbul. Combust.* **115** (4), 1435–1443.
- JIMENEZ, J. & MOSER, R. D. 2000 Large-eddy simulations: where are we and what can we expect? AIAA J. 38 (4), 605–612.
- Kawai, S. & Larsson, J. 2013 Dynamic non-equilibrium wall-modeling for large eddy simulation at high Reynolds numbers. *Phys. Fluids* **25** (1), 015105.
- Kerr, R. M., Domaradzki, J. A. & Barbier, G. 1996 Small-scale properties of nonlinear interactions and subgrid-scale energy transfer in isotropic turbulence. *Phys. Fluids* **8** (1), 197–208.
- Kobayashi, H. 2018 Improvement of the SGS model by using a scale-similarity model based on the analysis of SGS force and SGS energy transfer. *Int. J. Heat Fluid Flow* **72**, 329–336.
- Kobayashi, H. & Shimomura, Y. 2001 The performance of dynamic subgrid-scale models in the large eddy simulation of rotating homogeneous turbulence. *Phys. Fluids* **13** (8), 2350–2360.
- Larsson, J., Kawai, S., Bodart, J. & Bermejo-Moreno, I. 2016 Large eddy simulation with modeled wall-stress: recent progress and future directions. *Mech. Eng. Rev.* **3** (1), 15–00418.
- LEHMKUHL, O., PARK, G. I., Bose, S. T. & Moin, P. 2018 Large-eddy simulation of practical aeronautical flows at stall conditions. In *Proceedings of the 2018 Center for Turbulence Research Summer Program*, pp. 87–96.
- Li, Y. & Meneveau, C. 2004 Analysis of mean momentum flux in subgrid models of turbulence. *Phys. Fluids* **16** (9), 3483–3486.
- Ling, Y., Arranz, G., Williams, E., Goc, K., Griffin, K. & Lozano-Durán, A. 2022 Wall-modeled large-eddy simulation based on building-block flows. In *Proceedings of the 2022 Center for Turbulence Research Summer Program*, pp. 5–14.
- LIU, S., MENEVEAU, C. & KATZ, J. 1994 On the properties of similarity subgrid-scale models as deduced from measurements in a turbulent jet. *J. Fluid Mech.* 275, 83–119.
- Lozano-Durán, A. & Bae, H. J. 2019 Error scaling of large-eddy simulation in the outer region of wall-bounded turbulence. *J. Comput. Phys.* **392**, 532–555.
- Lund, T. S. & Novikov, E. A. 1992 Parameterization of subgrid-scale stress by the velocity gradient tensor. In *Center for Turbulence Research Annual Research Briefs*, pp. 27–43.
- Lund, T. S., Wu, X. & Squires, K. D. 1998 Generation of turbulent inflow data for spatially-developing boundary layer simulations. *J. Comput. Phys.* **140** (2), 233–258.
- MARSTORP, L., Brethouwer, G., Grundestam, O. & Johansson, A. V. 2009 Explicit algebraic subgrid stress models with application to rotating channel flow. *J. Fluid Mech.* **639**, 403–432.
- Meneveau, C. 1994 Statistics of turbulence subgrid-scale stresses: Necessary conditions and experimental tests. *Phys. Fluids* **6** (2), 815–833.

- MENEVEAU, C. & KATZ, J. 2000 Scale-invariance and turbulence models for large-eddy simulation. *Annu. Rev. Fluid Mech.* **32** (1), 1–32.
- MONTECCHIA, M., BRETHOUWER, G., JOHANSSON, A. V. & WALLIN, S. 2017 Taking large-eddy simulation of wall-bounded flows to higher Reynolds numbers by use of anisotropy-resolving subgrid models. *Phys. Rev. Fluids* **2** (3), 034601.
- Moser, R. D., Haering, S. W. & Yalla, G. R. 2021 Statistical properties of subgrid-scale turbulence models. *Annu. Rev. Fluid Mech.* 53 (1), 255–286.
- Park, G. I. 2017 Wall-modeled large-eddy simulation of a high Reynolds number separating and reattaching flow. *AIAA J.* **55** (11), 3709–3721.
- Park, G. I. & Moin, P. 2014 An improved dynamic non-equilibrium wall-model for large eddy simulation. *Phys. Fluids* **26** (1), 015108.
- Park, N., Yoo, J. Y. & Choi, H. 2005 Toward improved consistency of *a priori* tests with *a posteriori* tests in large eddy simulation. *Phys. Fluids* 17 (1), 015103.
- Prakash, A., Balin, R., Evans, J. A. & Jansen, K. E. 2024 A streamline coordinate analysis of a turbulent boundary layer subject to pressure gradients and curvature on the windward side of a bump. *J. Fluid Mech.* **984.** A23.
- RASAM, A., WALLIN, S., Brethouwer, G. & Johansson, A. V. 2017 Improving separated-flow predictions using an anisotropy-capturing subgrid-scale model. *Int. J. Heat Fluid Flow* **65**, 246–251.
- REZAEIRAVESH, S., MUKHA, T. & LIEFVENDAHL, M. 2019 Systematic study of accuracy of wall-modeled large eddy simulation using uncertainty quantification techniques. *Comput. Fluids* **185**, 34–58.
- SARGHINI, F., PIOMELLI, U. & BALARAS, E. 1999 Scale-similar models for large-eddy simulations. *Phys. Fluids* 11 (6), 1596–1607.
- Silvis, M. H. & Verstappen, R. 2019 Nonlinear subgrid-scale models for large-eddy simulation of rotating turbulent flows. In *Direct and large-eddy simulation XI*, pp. 129–134. Springer.
- SLOTNICK, J. P. 2019 Integrated CFD validation experiments for prediction of turbulent separated flows for subsonic transport aircraft. In Separated Flow: Prediction, Measurement and Assessment for Air and Sea Vehicles, STO Publication STO-MP-AVT-307-06.
- Smagorinsky, J. 1963 General circulation experiments with the primitive equations: I. the basic experiment. *Mon. Weather Rev.* **91** (3), 99–164.
- Spalart, P., Jansen, K. & Coleman, G. 2024 Direct numerical simulation of two boundary layers with the same pressure distribution but different surface curvatures. *arXiv* preprint arXiv:2409.00555.
- Uzun, A. & Malik, M. R. 2022 High-fidelity simulation of turbulent flow past Gaussian bump. AIAA J. **60** (4), 2130–2149.
- Uzun, A. & Malik, M. R. 2025 Application of a new nonlinear subgrid-scale model to a Gaussian bump flow. *AIAA J.* **63** (1), 354–360.
- Vollant, A., Balarac, G. & Corre, C. 2016 A dynamic regularized gradient model of the subgrid-scale stress tensor for large-eddy simulation. *Phys. Fluids* **28** (2), 025114.
- Van der Vorst, H. A. 1992 Bi-CGSTAB: A fast and smoothly converging variant of Bi-CG for the solution of nonsymmetric linear systems. *SIAM J. Sci. Comput.* **13** (2), 631–644.
- Vreman, B., Geurts, B. & Kuerten, H. 1994 On the formulation of the dynamic mixed subgrid-scale model. *Phys. Fluids* **6** (12), 4057–4059.
- VREMAN, B., GEURTS, B. & KUERTEN, H. 1997 Large-eddy simulation of the turbulent mixing layer. *J. Fluid Mech.* 339, 357–390.
- WANG, B. & BERGSTROM, D. J. 2005 A dynamic nonlinear subgrid-scale stress model. *Phys. Fluids* 17 (3), 035109.
- Wang, M. & Moin, P. 2002 Dynamic wall modeling for large-eddy simulation of complex turbulent flows. *Phys. Fluids* **14** (7), 2043–2051.
- WHITMORE, M. P., GRIFFIN, K. P., BOSE, S. T. & MOIN, P. 2021 Large-eddy simulation of a Gaussian bump with slip-wall boundary conditions. In *Center for Turbulence Research Annual Research Briefs*, pp. 45–58.
- WHITMORE, M. P., LOZANO-DURÁN, A. & MOIN, P. 2020 Requirements and sensitivity analysis of RANS-free wall-modeled LES. In *Center for Turbulence Research Annual Research Briefs*, pp. 97–108.
- WILLIAMS, O., SAMUELL, M., SARWAS, E. S., ROBBINS, M. & FERRANTE, A. 2020 Experimental study of a CFD validation test case for turbulent separated flows. In *AIAA Scitech 2020 Forum*, p. 0092.
- Xu, N. & Bermejo-Moreno, I. 2024 Wall-modeled large-eddy simulations of the flow over a Gaussian-shaped bump with a sensor-based blended wall model. *Phys. Rev. Fluids* **9** (11), 114605.

- Yang, Q. & Wang, M. 2013 Boundary-layer noise induced by arrays of roughness elements. *J. Fluid Mech.* **727**, 282–317.
- YANG, X. I. A. & GRIFFIN, K. P. 2021 Grid-point and time-step requirements for direct numerical simulation and large-eddy simulation. *Phys. Fluids* 33 (1), 015108.
- You, D., Ham, F. & Moin, P. 2008 Discrete conservation principles in large-eddy simulation with application to separation control over an airfoil. *Phys. Fluids* **20**, 101515.
- ZANG, Y., STREET, R. L. & KOSEFF, J. R. 1993 A dynamic mixed subgrid-scale model and its application to turbulent recirculating flows. *Phys. Fluids A* 5 (12), 3186–3196.
- Zhou, D. & Bae, H. J. 2024a Sensitivity analysis of wall-modeled large-eddy simulation for separated turbulent flow. *J. Comput. Phys.* **506**, 112948.
- Zhou, D. & Bae, H. J. 2024b Wall modeling of turbulent flows with varying pressure gradients using multi-agent reinforcement learning. AIAA J. 62 (10), 3713–3727.
- Zhou, D., Wang, K. & Wang, M. 2020 Large-eddy simulation of an axisymmetric boundary layer on a body of revolution. In *AIAA Aviation 2020 Forum*, p. 2989.
- Zhou, D., Wang, K. & Wang, M. 2024 Rotor aeroacoustic response to an axisymmetric turbulent boundary layer. *J. Fluid Mech.* **981**, A25.
- Zhou, D., Whitmore, M. P., Griffin, K. P. & Bae, H. J. 2023 Large-eddy simulation of flow over Boeing Gaussian bump using multi-agent reinforcement learning wall model. In *AIAA Aviation 2023 Forum*, p. 3985.
- Zhou, Z., Zhang, X., He, G. & Yang, X. 2025 A wall model for separated flows: embedded learning to improve *a posteriori* performance. *J. Fluid Mech.* **1002**, A3.